

ARMY RESEARCH LABORATORY



## **Aerodynamic Characterizations of Asymmetric and Maneuvering 105-, 120-, and 155-mm Fin-Stabilized Projectiles Derived From Telemetry Experiments**

by Frank Fresconi and Tom Harkins

ARL-TR-5495

April 2011

## **NOTICES**

### **Disclaimers**

The findings in this report are not to be construed as an official Department of the Army position unless so designated by other authorized documents.

Citation of manufacturer's or trade names does not constitute an official endorsement or approval of the use thereof.

Destroy this report when it is no longer needed. Do not return it to the originator.

# **Army Research Laboratory**

Aberdeen Proving Ground, MD 21005-5066

---

**ARL-TR-5495**

**April 2011**

## **Aerodynamic Characterizations of Asymmetric and Maneuvering 105-, 120-, and 155-mm Fin-Stabilized Projectiles Derived From Telemetry Experiments**

**Frank Fresconi and Tom Harkins  
Weapons and Materials Research Directorate, ARL**

<b>REPORT DOCUMENTATION PAGE</b>				<b>Form Approved OMB No. 0704-0188</b>	
<p>Public reporting burden for this collection of information is estimated to average 1 hour per response, including the time for reviewing instructions, searching existing data sources, gathering and maintaining the data needed, and completing and reviewing the collection information. Send comments regarding this burden estimate or any other aspect of this collection of information, including suggestions for reducing the burden, to Department of Defense, Washington Headquarters Services, Directorate for Information Operations and Reports (0704-0188), 1215 Jefferson Davis Highway, Suite 1204, Arlington, VA 22202-4302. Respondents should be aware that notwithstanding any other provision of law, no person shall be subject to any penalty for failing to comply with a collection of information if it does not display a currently valid OMB control number.</p> <p><b>PLEASE DO NOT RETURN YOUR FORM TO THE ABOVE ADDRESS.</b></p>					
1. REPORT DATE (DD-MM-YYYY)	2. REPORT TYPE			3. DATES COVERED (From - To)	
April 2011	Final			January 2008–October 2010	
<p><b>4. TITLE AND SUBTITLE</b> Aerodynamic Characterizations of Asymmetric and Maneuvering 105-, 120-, and 155-mm Fin-Stabilized Projectiles Derived From Telemetry Experiments</p>					
<p><b>6. AUTHOR(S)</b> Frank Fresconi and Tom Harkins</p>					
<p><b>7. PERFORMING ORGANIZATION NAME(S) AND ADDRESS(ES)</b> U.S. Army Research Laboratory ATTN: RDRL-WML-E Aberdeen Proving Ground, MD 21005-5069</p>					
<p><b>8. PERFORMING ORGANIZATION REPORT NUMBER</b> ARL-TR-5495</p>					
<p><b>9. SPONSORING/MONITORING AGENCY NAME(S) AND ADDRESS(ES)</b></p>					
<p><b>10. SPONSOR/MONITOR'S ACRONYM(S)</b></p>					
<p><b>11. SPONSOR/MONITOR'S REPORT NUMBER(S)</b></p>					
<p><b>12. DISTRIBUTION/AVAILABILITY STATEMENT</b> Approved for public release; distribution is unlimited.</p>					
<p><b>13. SUPPLEMENTARY NOTES</b></p>					
<p><b>14. ABSTRACT</b> Accurate knowledge of candidate projectiles' aerodynamics is crucial for successful development of tube- and gun-launched precision munitions. This is especially true when control authority is low, as is often the case with rolling projectiles. In these instances, truth models of the projectiles' flight characteristics need to be of sufficient quality to enable the guidance, navigation, and control (GNC) system to produce efficient corrective maneuvers. Recently, the U.S. Army conducted instrumented flight experiments to quantify aerodynamics and flight dynamics for three U.S. Army precision munitions programs. These projectiles were of different shapes and calibers (105, 120, and 155 mm), but similar in having supercaliber, roll-inducing tailfins and employing nose-mounted canards as their maneuver control mechanisms. In this effort, for the first time, aerodynamic terms for precision airframes and control mechanisms were estimated from data acquired from projectile on-board instrumentation via elevated gun firings. Observations of these complexities were possible because data were collected for the entire free flights of these projectiles encompassing varying Mach numbers and dynamic conditions not previously examined, thereby complementing the pre-flight analyses and reducing cost by enabling characterization of more aerodynamic parameters with less testing.</p>					
<p><b>15. SUBJECT TERMS</b> fin-stabilized projectiles, telemetry, asymmetric, maneuvering, aerodynamics</p>					
<p><b>16. SECURITY CLASSIFICATION OF:</b></p>			<p><b>17. LIMITATION OF ABSTRACT</b></p>	<p><b>18. NUMBER OF PAGES</b></p>	<p><b>19a. NAME OF RESPONSIBLE PERSON</b> Frank Fresconi</p>
a. REPORT	b. ABSTRACT	c. THIS PAGE			UU

Standard Form 298 (Rev. 8/98)

Prescribed by ANSI Std. Z39.18

---

## Contents

---

<b>List of Figures</b>	<b>iv</b>
<b>List of Tables</b>	<b>vi</b>
<b>Acknowledgments</b>	<b>vii</b>
<b>1. Introduction</b>	<b>1</b>
<b>2. Experimental Setup</b>	<b>2</b>
2.1 Projectile Descriptions .....	2
2.2 Projectile On-Board Instrumentation .....	5
2.3 Firing Ranges and Instrumentation .....	6
<b>3. Flight Data Processing Methodology</b>	<b>9</b>
<b>4. Results</b>	<b>10</b>
4.1 The 105-mm Flight Dynamics: VAPP-7.....	11
4.2 The 105-mm Flight Dynamics: VAPP-8.....	14
4.3 VAPP-7 and VAPP-8 Aerodynamic Coefficients.....	18
4.4 The 120-mm Flight Dynamics: VAPP-13.....	21
4.5 VAPP-13 Aerodynamic Coefficients .....	23
4.6 The 155-mm Flight Dynamics: VAPP-23.....	25
4.7 The 155-mm Flight Dynamics: VAPP-24.....	27
4.8 The 155-mm Flight Dynamics: VAPP-25.....	30
4.9 VAPP-23, 24, and 25 Aerodynamic Coefficients .....	32
4.10 Dynamic Stability of 155-mm Projectile.....	35
<b>5. Conclusions</b>	<b>37</b>
<b>6. References</b>	<b>39</b>
<b>Distribution List</b>	<b>41</b>

---

## List of Figures

---

Figure 1. The 105-mm airframe.....	3
Figure 2. The 120-mm airframe.....	4
Figure 3. The 155-mm airframe.....	4
Figure 4. Sensor suite and DSP stack .....	5
Figure 5. Smoothbore 8-in gun at the ARL TEF .....	6
Figure 6. The 120-mm mortar tube at the ATC range.....	7
Figure 7. Paladin with 155-mm cannon at YPG.....	8
Figure 8. Experimental and calculated radar data for VAPP-7.....	12
Figure 9. Experimental and calculated solar data for VAPP-7.....	12
Figure 10. Reconstructed angular motion for VAPP-7.....	13
Figure 11. Experimental and calculated radar data for VAPP-8 .....	15
Figure 12. Experimental and calculated accelerometer and solar data for VAPP-8.....	16
Figure 13. Reconstructed angular motion for VAPP-8.....	18
Figure 14. Aerodynamic coefficients for the 105-mm airframe.....	19
Figure 15. More aerodynamic coefficients for the 105-mm airframe (VAPP-8) .....	21
Figure 16. Experimental and calculated radar data for VAPP-13 .....	22
Figure 17. Experimental and calculated magnetic data for VAPP-13.....	22
Figure 18. Reconstructed angular motion for VAPP-13.....	23
Figure 19. Aerodynamic coefficients for 120-mm airframe.....	24
Figure 20. Experimental and calculated radar data for VAPP-23 .....	25
Figure 21. Experimental and calculated accelerometer, solar, and magnetic data for VAPP-23.....	26
Figure 22. Reconstructed angular motion for VAPP-23.....	27
Figure 23. Experimental and calculated radar data for VAPP-24 .....	28
Figure 24. Experimental and calculated accelerometer, solar, and magnetic data for VAPP-24.....	29
Figure 25. Reconstructed angular motion for VAPP-24.....	30
Figure 26. Experimental and calculated radar data for VAPP-25 .....	31
Figure 27. Experimental and calculated accelerometer and solar data for VAPP-25.....	31
Figure 28. Reconstructed angular motion for VAPP-25.....	32
Figure 29. Aerodynamic coefficients for 155-mm airframe.....	34

Figure 30. Dynamic side moment coefficient for 155-mm airframe.....35

Figure 31. Dynamic instability metrics for 155-mm airframe.....37

---

## **List of Tables**

---

Table 1. Physical properties of projectiles.....	5
Table 2. Launch conditions.....	8
Table 3. Order of magnitude of fit metric for acceptable results.....	10

---

## **Acknowledgments**

---

The authors would like to gratefully acknowledge the contributions of Wayne Hathaway at Arrow Tech Associates in Burlington, VT, for providing information on parameter identification methodology and aerodynamics reduction support.

INTENTIONALLY LEFT BLANK.

---

## 1. Introduction

---

Many different kinds of airframe geometries are being investigated for use as precision munitions throughout the armed services. Within the U.S. Army, rolling projectiles using movable lifting surfaces for maneuver control are being developed (1). The aerodynamic characterization of such projectiles is more difficult than characterization of traditional symmetric ballistic projectiles. Because these control mechanisms produce aerodynamic asymmetries and flow interactions, more sophisticated aerodynamic models and flight dynamics analyses are required that include these phenomena (e.g., roll angle dependent pitching moments and normal forces). Thorough understanding of the flight behavior of such projectiles is necessary to successfully guide them to desired points in space.

Accurate aerodynamic characterization is important because each of the precision munitions examined in this effort had performance goals of maneuverability, roll rate, and dynamic stability. Many tools support the initial design and further refinement of aerodynamics for precision munitions. Semi-empirical aeroprediction, wind tunnel testing, computational fluid dynamics (CFD), and free-flight experiments were all employed during the overall programs to assess the aerodynamics of the 105-, 120-, and 155-mm fin-stabilized airframes discussed herein. The results of the present work permit an assessment of the quality of the various airframe designs.

This effort includes analyses of six flight experiments. Though there are three distinct types of projectiles, they are all designated by the name “VAPP,” followed by a numeral. This naming convention arises from the use on all these projectiles of the same maneuver mechanism of a single opposed pair of nose-mounted canards. Particular component dimensions vary among the three projectiles but the mechanisms are essentially the same. This system was designed and built at the U.S. Army Research Laboratory (ARL) as part of the Very Affordable Precision Projectile (VAPP) program, and the numerals in the names reflect the sequential embodiments in flight experiment hardware.

When properly employed the different aerodynamic techniques are not competitors but complementary contributors with each technique supplying critical information for the high fidelity aerodynamic characterization necessary to perform successful guide-to-hit flight experiments (1, 2). The wind tunnel and predictive computational efforts will be reported separately.

The focus of this report is experimental determination of projectile aerodynamics from elevated gun firings. To accomplish this, projectiles and firing ranges are instrumented to obtain measurements of the projectile motion throughout its trajectory. These data are used in a parameter identification algorithm known as the maximum likelihood method with differential

corrections to quantify aerodynamic coefficients. This analysis is conducted within the Extending Telemetry Reduction to Aerodynamic Coefficients and Trajectory Reconstruction (EXTRACTR) software. The EXTRACTR methodology, its validation, and past applications have been documented previously (3–6).

The novel contribution of the present effort lies in characterizing aerodynamics associated with the precision projectile and control mechanism (notably asymmetries and canard terms) via data collected during ballistic and maneuvering free-flights. The increased dimensionality of this characterization versus the characterization of symmetrical, non-maneuvering flight bodies makes for a more difficult technical task. This is due to the need for obtaining a greater volume of experimental data to reflect the added dependencies combined with the presence of nonlinearities within the underlying aeroballistic theory.

This report will proceed by first covering the experimental procedures to include descriptions of the test projectiles and the test instrumentation both on-board the projectiles and at the firing ranges. Next, data collection and post-flight analysis of these data leading to projectile motion history reconstructions will be covered including discussion on the quality of the results. Finally, the aerodynamic coefficients that reproduce the experimental flight motions are provided.

---

## 2. Experimental Setup

---

### 2.1 Projectile Descriptions

All three projectile types were fin-stabilized with tail-mounted super-caliber fins. When tactically operational, the 105- and 155-mm precision munitions will be launched from rifled artillery tubes and utilize slip-band obturators to ensure low spin at launch. The 120-mm munition will be launched from a smoothbore mortar. In all cases, the tail fins will deploy after launch and are canted or beveled to provide roll torque. The respective fin configurations were designed to achieve a balance between aerodynamic roll torque and roll damping yielding a steady state roll rate avoiding roll-yaw resonance and conducive for guidance, navigation, and control GNC system functionality. All projectiles rolled in accordance with the right-hand rule with the vector pointing out the nose.

All three projectile types employ a single opposed pair of nose-mounted canards as maneuver mechanisms. The two canards are mounted on a common rotation axis so that they always lie in the same plane. When affecting a maneuver, the canards are actuated in a sinusoidal manner with their period equal to the projectile roll period. The maximum allowable deflection angle of the canards is  $\pm 10^\circ$ , where  $0^\circ$  is defined by the canards and the projectile spin axis being coplanar. The period of canard actuation is matched to the roll cycle of the projectile so that the lift resulting from any canard deflection angle is always in the same inertial direction thereby

achieving a maneuver in that direction. This simple single-axis control actuation system (CAS) with a rolling airframe is less costly than other precision munition maneuver concepts in these calibers known to the authors.

Placement of canards in a single plane introduces an aerodynamic asymmetry that complicates the projectiles' aerodynamic characterizations and flight dynamics. The normal force is greater and the aerodynamic center-of-pressure (CP) moves nose ward in the plane of roll defined by the projectile rotation axis and the canard pivot axis as compared to a plane  $90^\circ$  away (i.e., the plane of roll perpendicular to the canard axis). Assessment of aerodynamics is further complicated because course-correcting maneuvers can potentially be commanded anytime in flight, requiring canard deflections that dynamically change the normal force and center of pressure at a range of Mach numbers, angles of attack, and any roll orientation. These asymmetry considerations apply to all three of the subject projectiles.

A photograph of the 105-mm projectile hardware is shown in figure 1. For the flight experiments treated herein, these projectiles were launched from a smoothbore 8-in gun in a sabot-pusher-plate obturator package. This allowed the use of fixed tail fins of the tactical design geometry. When launched from a 105-mm tube, these six fins need to deploy post launch. Each fin had a full cant of  $1.25^\circ$ . The tip-to-tip span of the maneuver canards is just under 105 mm. This airframe was designed using aeroprediction, CFD, and a series of dynamic wind tunnel experiments with the CAS to achieve maximum aerodynamic control with minimal hinge loading within the allowable design space (and corresponding minimal battery power requirement). Physical characteristics of this airframe were measured prior to firing and are given in table 1.



Figure 1. The 105-mm airframe.

A high-speed camera image of the 120-mm airframe in free-flight is given in figure 2. These projectiles were launched from the standard 120-mm smoothbore mortar tube. The four tail fins on this projectile were super-caliber, forward-folding with leading and trailing edge bevel. Various boom lengths were explored in the wind tunnel to determine the static stability. A slightly longer boom than the inventory M934 mortar projectile was used. The body of this

projectile was also longer than the M934, providing more normal force. Canards were identical to those on the 105-mm projectile. Wind tunnel (7) and CFD techniques were utilized to assess aerodynamics before gun firings. Table 1 gives the physical properties of the 120-mm mortar round.

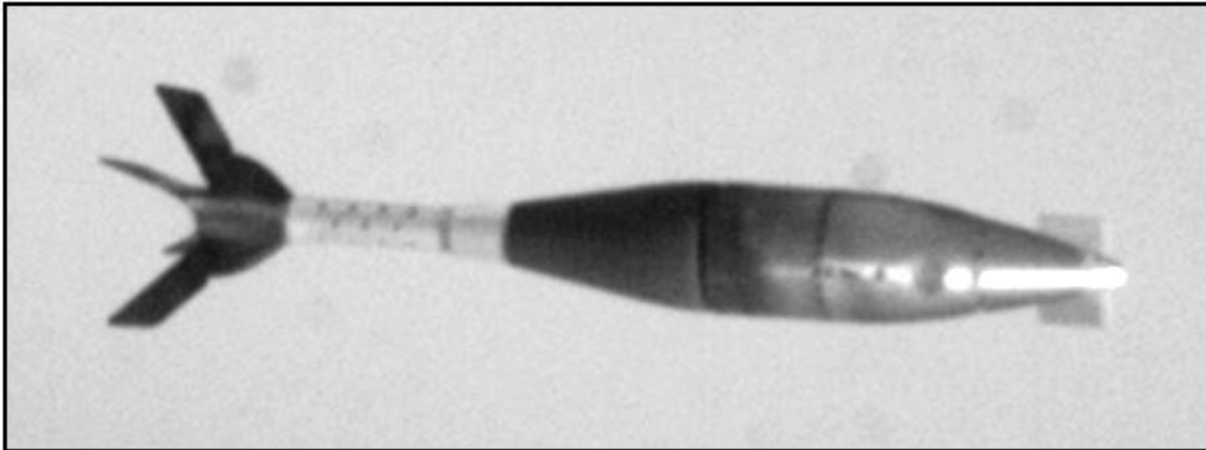


Figure 2. The 120-mm airframe.

Figure 3 shows the 155-mm projectile in free-flight. These projectiles were launched from a rifled 155-mm tube. The eight tail fins each featured a beveled leading edge and bent outer-corner trailing edge to supply the necessary roll torque. These fins were deployed post-launch. A series of wind tunnel tests were conducted to evaluate the canards, fin cant, and center of pressure location. The canards were different than the 105- and 120-mm airframes to enable maneuvers at higher Mach number. Physical properties of the 155-mm projectile are given in table 1.



Figure 3. The 155-mm airframe.

Table 1. Physical properties of projectiles.

Projectile (mm)	Mass (kg)	Axial Inertia (kg m <sup>2</sup> )	Transverse Inertia (kg m <sup>2</sup> )	Center of Gravity From Nose (mm)	Overall Length (mm)
105	18.533	0.0333	0.7005	400.4	759.6
120	18.240	0.0370	0.5260	349.2	893.5
155	44.197	0.1664	2.2712	597.6	981.4

## 2.2 Projectile On-Board Instrumentation

Each projectile was instrumented with a similar strap-down sensor package to derive flight motions. The sensor suite consisted of a three-axis magnetometer, 2 solar sensors (installed 180° apart circumferentially), 6 angular rate sensors (2 sensors with different ranges parallel to each principal axis), and 10 linear accelerometers (2 with different ranges parallel to each principal axis and 4 positioned symmetrically about the spin axis with signals summed to provide an estimate of centripetal acceleration). All save the solar sensors were mounted within a stack like that shown in figure 4. These stacks also featured a digital signal processor (DSP) that sampled the sensors on an analog-to-digital converter and populated a pulse code modulated stream which was then broadcast by an onboard S-band telemetry transmitter and antenna. These sensors and electronics were integrated into the projectile body and an epoxy potting material was used to ensure structural integrity during gun launch. The telemetry data streams were received and recorded real-time at multiple ground stations along the respective trajectories to ensure complete data capture. The data were demodulated and processed post-flight in conjunction with the data provided by the range instrumentation discussed in the next section.

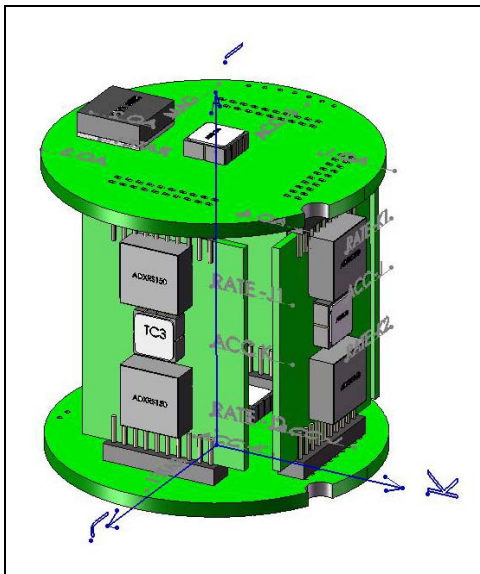


Figure 4. Sensor suite and DSP stack.

### 2.3 Firing Ranges and Instrumentation

Flight experiments of the three projectile types took place at three different test ranges. However, similar ballistic range instrumentation was used for all the flight experiments consisting of tracking and fixed radars, high-speed photography, gun pressure measurements, and multiple telemetry ground stations. All experiment assets were positioned at surveyed locations. Meteorological data were recorded with both ground and balloon-carried instruments throughout the test events.

The 105-mm projectile gun firings were conducted at ARL's Transonic Experimental Facility (TEF) on the Aberdeen Proving Ground (APG). The 120-mm firings were conducted at the Aberdeen Test Center (ATC) Ballistic and Romney Creek Ranges, also at APG. The 155-mm firings were conducted at Gun Position 2490R on the Yuma Proving Ground (YPG). The guns used for these different firings are shown in figures 5–7. The individual projectile designations and launch conditions for the flights of the six rounds analyzed in this report are given in table 2.



Figure 5. Smoothbore 8-in gun at the ARL TEF.



Figure 6. The 120-mm mortar tube at the ATC range.



Figure 7. Paladin with 155-mm cannon at YPG.

Table 2. Launch conditions.

Projectile ID No.	Diameter (mm)	Date/Time-of-Fire (GMT)	Quadrant Elevation (deg)	Launch Velocity (m/s)
VAPP-7	105	13 Dec – 16:54	15	289
VAPP-8	105	24 Jan – 18:14	15	291
VAPP-13	120	26 Feb – 18:42	62	232
VAPP-23	155	10 Jun – 21:48	50	572
VAPP-24	155	10 Jun – 22:46	50	695
VAPP-25	155	11 Jun – 00:02	50	694

---

### 3. Flight Data Processing Methodology

---

Simply put, the task intended to be performed by the parameter identification algorithm is to determine values of the aerodynamic coefficients appearing in the force and moment formulation of the 6 degrees-of-freedom (6-DOF) differential equations of motion that reproduce the observed dynamic states of that projectile in the free-flight experiments. Time histories of twelve projectile states are necessary to fully describe a trajectory: three components of position, three components of translational rates, three components of angular orientation, and three components of angular rates. Environmental parameters along the flight path also affect projectile dynamics, e.g., temperature, winds, etc.

The primary off-projectile data used for estimating aerodynamic coefficients are the meteorological data and three measurements obtained with the tracking radar (i.e., the projectile radial velocity, radar elevation angle, and radar azimuth angle). The primary strapdown-sensor-derived data used for estimating aerodynamic coefficients are the projectile's solar aspect angle, solar roll rate, magnetic aspect angle, and magnetic roll rate (defined herein). In a few cases, projectile spin rates obtained from the centripetal acceleration estimate described earlier were also used.

Calibrations were performed on the sensors prior to the flight experiments. The two solar sensors were excited with light while undergoing prescribed motions to accurately determine the orientations of these sensors as installed on each of the test projectiles. Analogously, the magnetic sensors' biases, scale factors, and installed orientations were determined using a least squares fitting technique on the magnetometers output for a prescribed set of Helmholtz-coil-generated magnetic fields systematically varied in strength and orientation relative to the projectile-installed sensor stacks (8).

These calibrations enabled the metrics of interest to the experimental aerodynamics technique to be calculated in appropriate engineering units. The solar and magnetic roll rates are estimates of projectile roll rates with respect to the sun and the local geomagnetic field respectively. The solar aspect angle is the included angle between two vectors originating at the projectile's center of gravity (CG). The first is co-linear with the projectile's roll axis and directed through the nose and the second is directed towards the sun. The magnetic aspect angle is the included angle between the roll axis vector and a vector originating at the CG and parallel to the local geomagnetic field. Methodologies employed to obtain these and other airframe states and other available body-fixed measurements during flight experiments have been documented elsewhere (9, 10).

The radar, solar, and magnetometer data were assembled along with the firing log, projectile mass properties, initial aerodynamic estimates, survey, and meteorological data for each flight.

Coefficient values were estimated that would achieve fits to the measured motion when inserted into the fully nonlinear 6-DOF equations of motion. Many of the individual fits were performed using only limited portions of a flight experiment's dynamic states estimates. Primarily, this is done for one of several reasons. In some instances, the dynamics necessary to observe the effects of a particular desired parameter only occur for limited portions of the trajectory, e.g., yawing motion must be occurring to estimate a projectile's pitching moment. In other cases, some projectile state may be applicable to only a portion of a trajectory, e.g., transonic velocity. In yet other cases, pronounced observable projectile dynamics might be present but the potential aerodynamic parameters underlying these states may be ambiguous. Additionally, the degree of difficulty associated with performing simultaneous multiple parameter identifications with potentially over fifty possible parameters, nonlinear flight dynamics, and experimental data which may not include the complete 12 projectile states for every desired flavor of projectile dynamics prevents automation of the analyses. Typical aerodynamic coefficient estimations proceed sequentially with an experienced aero ballistian matching appropriate portions of experimental data and parameter determinations in a hierarchical order.

Root-sum-of-squares (RSS) differences between the experimental observations and 6-DOF-calculated predictions of projectile states (e.g., radial velocity, magnetic aspect angle) provide a measure of the fit accuracy of the parameter identification process to the experimental data. Achievable accuracies of the experimental measurements dictate appropriate levels of the RSS differences between the experimental and calculated projectile states. The orders-of-magnitude of fit metrics for all analyses reported in this effort fall within the acceptable regimes (discussed in Davis et al. [5]) given in table 3.

Table 3. Order of magnitude of fit metric for acceptable results.

RSS Fit Metric	Order of Magnitude
Radial velocity	1. m/s
Radar elevation	0.1 deg
Radar azimuth	0.1 deg
Solar roll	0.1 rad/s
Solar aspect angle	0.1 deg
Magnetic roll rate	0.1 rad/s
Magnetic aspect angle	0.1 deg

---

## 4. Results

---

Estimated aerodynamic coefficients were non-dimensionalized using the diameter-referenced cross-sectional area of each projectile type ( $A = \pi D^2/4$ ). Discussion of the six test rounds will be sequential and will be similar in covering the experimental and 6-DOF-calculated vehicle

states being matched, the resulting reconstructed angular motion histories, and the aerodynamic coefficients found necessary to achieve those matches.

#### **4.1 The 105-mm Flight Dynamics: VAPP-7**

The first flight experiment to be discussed is that of one of the 105-mm artillery rounds, designated as VAPP-7. In this experiment, some of the maneuver mechanism timing and electronic functions were tested but no canard deflections were implemented. Hence, the flight of VAPP-7 was ballistic. Radar and solar data suitable for analysis were obtained in this experiment. As noted previously, the “influence” of some aerodynamic parameters can only be analyzed when projectiles are undergoing appropriate dynamics. This is particularly true of angle-of-attack-dependent parameters where a necessary condition for performing the nonlinear 6-DOF analysis is angular motion of an appropriate kind with adequate magnitude. For this reason, distinct parameter identification analyses were conducted on two subsets of the flight data. Launch disturbances induced pronounced angular motion at muzzle exit that damped to less than  $1^\circ$  within 1 s. Later in flight, throughout the interval from 5 to 7.5 s, angular coning motion of constant frequency and amplitude occurred. Comparisons of the experimental radar and solar data for these two intervals with those calculated through the parameter identification process are presented in figures 8 and 9 and suggest good agreement. In fact, the fit metrics met the criteria given in table 3. The roll rate was not fit well late in flight, therefore, these results are not presented, and static and dynamic roll moments were not included at this Mach number.

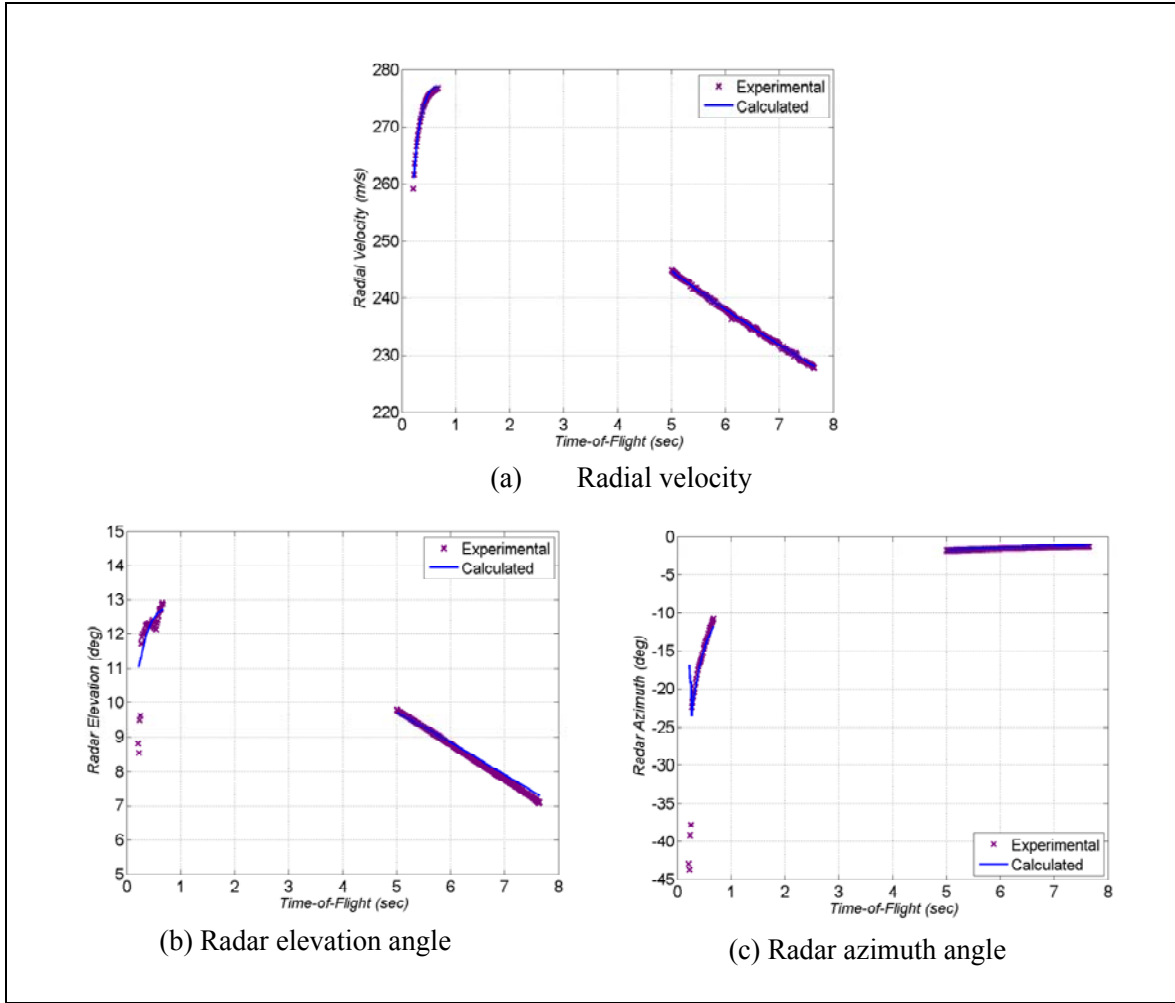


Figure 8. Experimental and calculated radar data for VAPP-7.

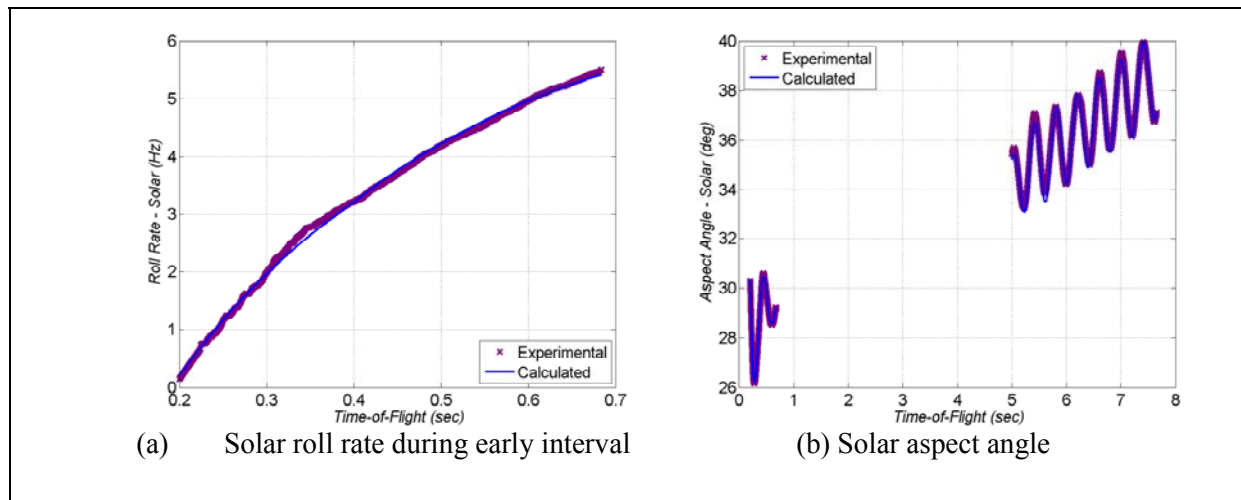


Figure 9. Experimental and calculated solar data for VAPP-7.

Matching the experimental data with 6-DOF calculations permits a reconstruction of complete angular flight motion. All ensuing discussion of angular motion assumes the observer sits behind the projectile looking down the longitudinal axis. The pitch angle-of-attack,  $\alpha$ , is defined as positive nose up and the yaw angle-of-attack,  $\beta$ , is positive nose right. Total angle-of-attack is the RSS of the pitch and yaw angles-of-attack. Figure 10 presents the reconstructed VAPP-7 angular motion early and late in flight. Projectile launch disturbances resulted in an approximately  $7^\circ$  maximum total angle-of-attack. This angle-of-attack magnitude decreased to less than  $1^\circ$  within 1 s in a clockwise oriented spiral pattern. In all angular motion reconstructions provided in this effort, an “o” represents the angular state at the initial time and an “x” represents the angular state at the final time. Beginning approximately 4 s after launch, total angle-of-attack grows to about  $1.5^\circ$  in 1 s and remains fairly regular for a time. This interval’s solar aspect angle history was fit by introducing a positive static side moment coefficient in the aerodynamic model.

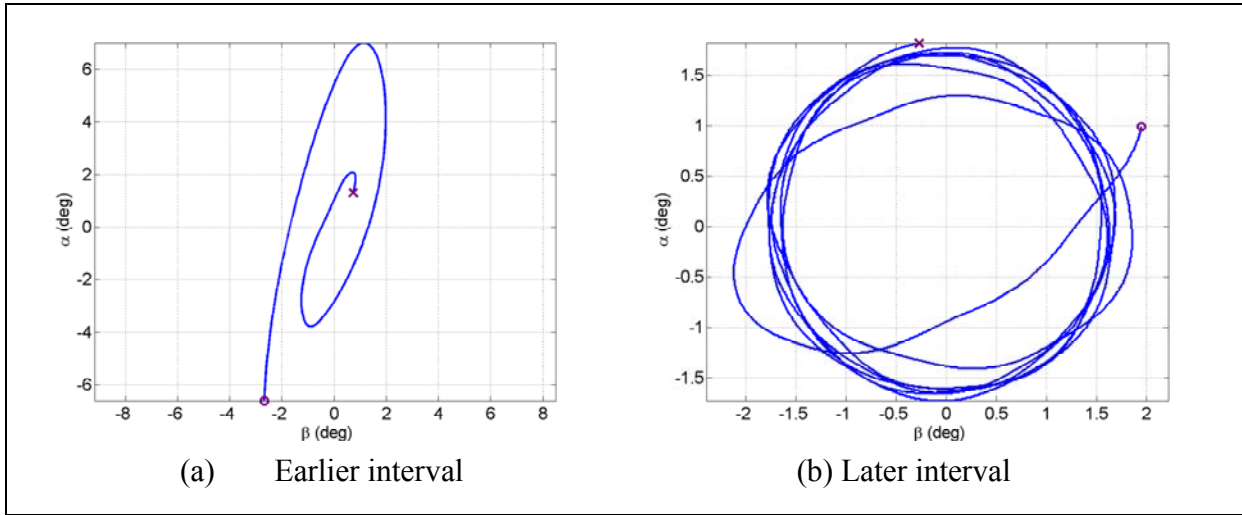


Figure 10. Reconstructed angular motion for VAPP-7.

Utilizing a side moment in the model requires a general discussion of uniqueness of the aerodynamic parameter identification solution. The manner in which the aerodynamic model is constructed and the range of experimental measurements that are available can prohibit some parameters from being uniquely determined. This was problematic for parameters associated with the amplitude of angle-of-attack of VAPP-7. Pitch damping, static side moment, and dynamic side moment can all contribute to angle-of-attack magnitude and be indistinguishable without additional information.

Furthermore, side moments produce coning motion. The action of a side moment is to induce angular motion  $90^\circ$  out of phase with the instantaneous pitch and yaw angle-of-attack. An instant later, pitch and yaw angle-of-attack have rotated slightly in response to the side moment

and the direction of the side moment has rotated by the same amount. This activity proceeds at the yawing rate of the airframe producing motion where the projectile nose circumscribes a complete circle in a single yaw cycle (or, alternatively, the projectile spin axis orientation forms a cone when considering the pitching and yawing motion hinged about the CG).

For fin-stabilized projectiles, the relative effects of the static and dynamic side moments prescribe the sense of coning motion (clockwise or counter-clockwise). Static side moments scale with angle-of-attack and dynamic side moments go with both angle-of-attack and roll rate. Thus, measurements of coning rate, coning direction, steady roll rate, and transient roll rate are required in each Mach regime to fully differentiate and characterize the side moments.

When both solar and magnetic aspect angle histories are available and the solar, magnetic, and roll axis vectors are not coplanar, the sense of the coning motion can be resolved with the analysis tools of the present work. An independent validation of the coning motion was also undertaken for some cases using the vector matching technique termed POINTER (Projectile Orientation In Navigation TERms – U.S. patent 6398155 [11]) described in Hepner and Harkins (12) and Harkins (13).

Because magnetic aspect data were not obtained for the VAPP-7 flight, the coning direction could not be determined. However, CFD predictions and wind tunnel measurements filled in some of the gaps not observed in the flight experiments to assess side moments for different projectiles examined in this work. For VAPP-7, CFD supported the choice of the dominance of a static side moment and a clockwise coning direction and this choice provided the best fit to the experimental data.

## 4.2 The 105-mm Flight Dynamics: VAPP-8

In this experiment, a maneuver intended to extend the range of the VAPP-8 projectile was initiated approximately 2 s after gun launch. Thereafter, the canards were continuously deflected sinusoidally to positive and  $-10^\circ$  at the roll frequency of the projectile. To achieve maximum range extension, the relative phasing of the canard deflection period and the projectile roll orientation period needed to be such that the canard-deflection-generated lift was oriented upwards. The appropriate timings of the canard deflection commands were formed using the solar sensors to determine the inertial roll orientation and roll rate of the projectile in flight. Radar, accelerometer, and solar data were obtained from the flight experiment and employed for aerodynamics estimation.

The canard deflection history, monitored and inserted into the telemetry stream by the DSP, was an additional source of data input to the parameter identification methodology. In order to use these data, it was necessary to extend the methodology by including a more sophisticated aerodynamic model that enabled the control-mechanism-related parameters to be estimated. These advances enabled the canard normal force coefficient and the longitudinal CP location of the canards to be assessed.

All fits to experimental data for VAPP-8 met the quality criteria of table 3. The experimental and calculated radar data for the flight are in figure 11. Figure 11b includes not only the measured and calculated radar elevation angles of the VAPP-8 trajectory, but also the model-predicted radar elevation angle history if there had been no maneuver. For such a ballistic flight, the predicted elevation data reflects a standard, exponentially-damped, parabolic ballistic trajectory. However, for the maneuvering, range-extending VAPP-8 flight, the elevation angle decay rate is greatly reduced from that of the predicted ballistic flight, evidencing successful range extension maneuver implementation.

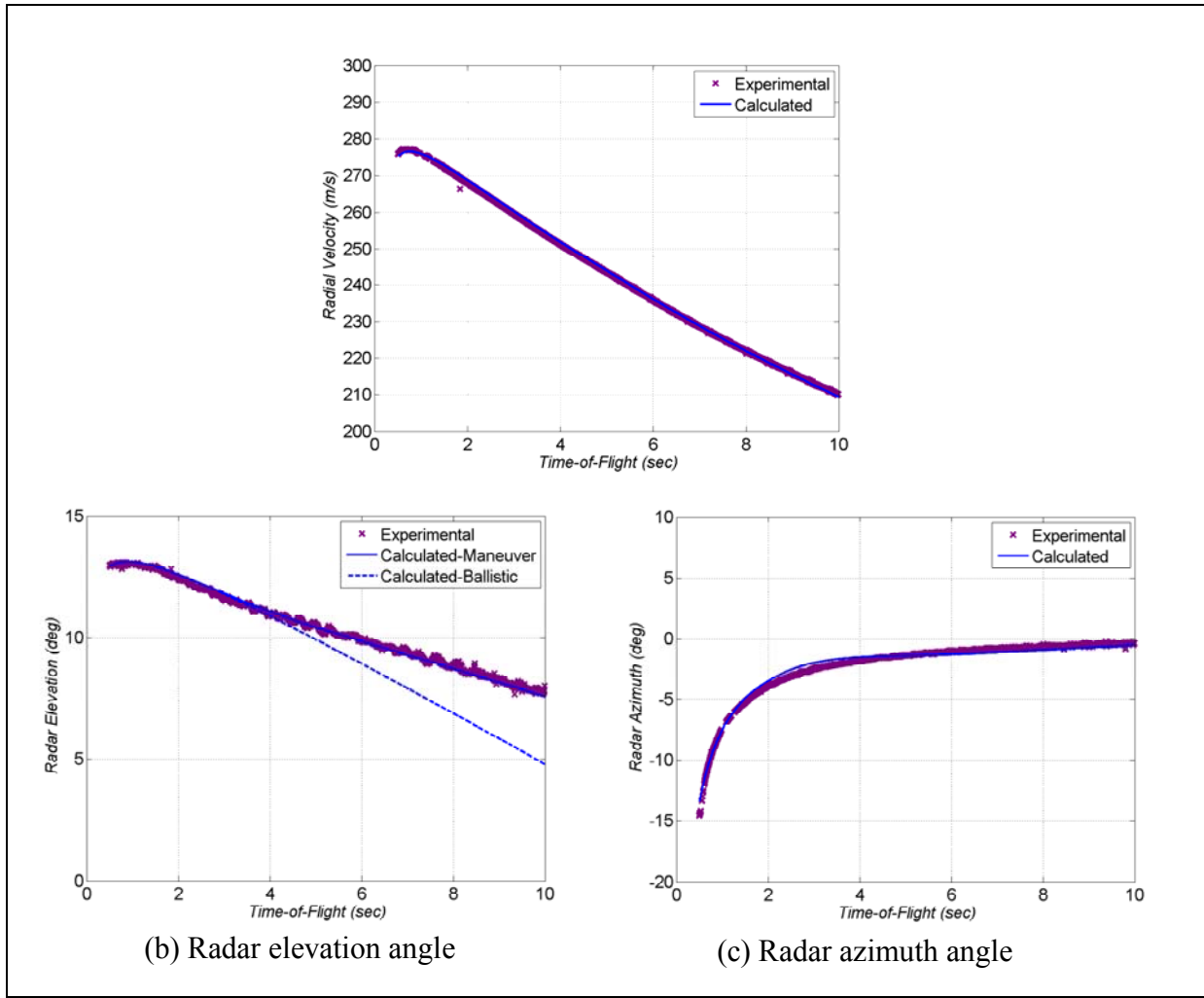


Figure 11. Experimental and calculated radar data for VAPP-8

Some low-magnitude oscillatory center-of-gravity motion is evident in the radar elevation data (e.g., between 4 and 6 s in figure 11b). This measured swerve motion is likely produced by oscillatory angular motion (coning) at the yaw rate. The centroid of the radar return is changing due to the coning motion.

Observable changes in the CG from the ballistic flight enable the normal force of the projectile to be evaluated in the parameter identification process. The normal force is usually indeterminable for ballistic flights since the angle-of-attack is too small and the radar data is of insufficient accuracy. For the maneuver flight of the 105-mm airframe, the mean and fluctuating components of the CG motion were appreciable enough to support estimates of the projectile normal force from elevated gun firings for the first time.

The roll rate and solar aspect angle data are provided in figure 12. The roll-rate estimate (figure 12a) was obtained from the four accelerometer constellation described previously. The oscillations in the latter portion of the roll rate history are at the yawing frequency and reflects the fact that the accelerometer constellation output is proportional to  $\left( p^2 + \frac{r^2 + q^2}{2} \right)$ , see Hepner and Hawkins (12).\*

Hepner and Hawkins (12).\*

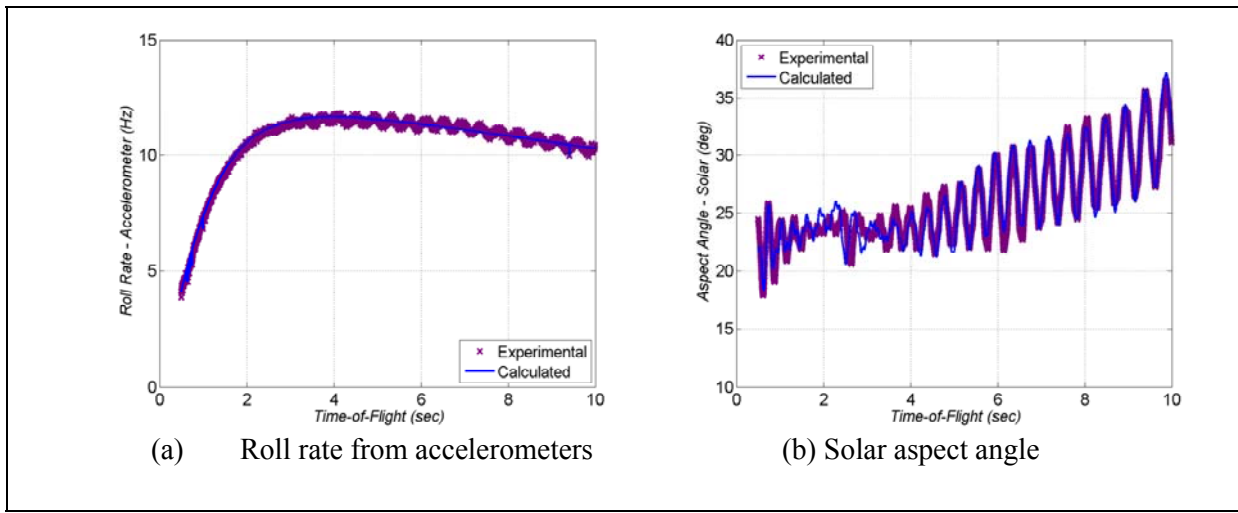


Figure 12. Experimental and calculated accelerometer and solar data for VAPP-8.

The solar aspect angle history (figure 12b) shows the angular motion for the ballistic and maneuver portions of the flight. Launch disturbances damped to less than 1 deg total angle-of-attack prior to initiation of the canard deflections. Shortly before 2 s, canard deflections began and continued thereafter. A poor match is seen between the measured and 6-DOF-predicted solar aspect angles for approximately the first 1.5 s of canard operations but a good match thereafter. During this interval of transition between ballistic and maneuvering flight, the current model does not fully characterize the angular motion. The timing of control events in the yaw and roll cycles during transient phenomena may be crucial to improving the comparison. Further work to accomplish such characterizations is clearly desirable but beyond the scope of this effort. The important observation for this effort is that the flight dynamics were adequately characterized to enable flight control development.

\* In the equation,  $p$ ,  $q$ ,  $r$  are the projectile's roll, pitch, and yaw angular rates, respectively.

Because the velocity histories of VAPP-7 and VAPP-8 are nearly identical, data from similar time intervals can be compared. In the 57-s interval of the solar angle histories of VAPP-7 (ballistic) and VAPP-8 (maneuvering), both projectiles have matching yaw frequencies. However, the magnitude of the yawing motion of VAPP-8 is approximately twice that of VAPP-7. A positive static side moment coefficient was used in the modeling of the VAPP-8 coning motion since this was shown to provide the best fit for the VAPP-7 ballistic flight. It is not inconceivable that a dynamic side moment may also contribute to the angular motion. Aerodynamic trim moments were included to improve the fit to the experimental solar aspect angle for VAPP-8.

The VAPP-8 angle-of-attack behaviors are further exemplified in the angular motion reconstructions of figure 13. The ballistic phase of the flight is given in figure 13a. The first point in this reconstruction is of the heading at the first solar observation approximately 0.4 s after muzzle exit. At this time, the nose of the projectile was yawed about  $2^\circ$  up and about  $2.5^\circ$  to the right. Thereafter, the yaw magnitude decreased to less than 1 deg total angle-of-attack before the maneuver onset. Visual examination of  $\alpha$  and  $\beta$  for the final yaw cycle in this interval shows a near zero average angle of attack. The complicated early structure of the curve in figure 13a (seen as scalloped shapes) reflects the addition of the trim moment to the aerodynamic model.

The maneuver portion of the VAPP-8 flight is shown in figure 13b. Approximately  $3^\circ$  average of angle-of-attack was produced by the control mechanism (mean  $\alpha \sim 3^\circ$  and  $\beta \sim 1.5^\circ$ ). An elliptically-skewed coning motion with amplitude near  $3^\circ$  is apparent. This complex coning motion was due to the interaction of trim and side moments, and the control mechanism. VAPP-8's coning motion in figure 13b is mainly due to the static side moment. Comparing the coning amplitude of about  $1.5^\circ$  for the ballistic flight (figure 10b) with the  $3^\circ$  amplitude for the maneuver flight (figure 13b) underscores the behavior of the dynamic instability. Static side moment magnitude scales with the total angle-of-attack. Total angle-of-attack was higher for the maneuver flight than the ballistic flight due to the action of the control mechanism. For this reason the static side moment is larger and therefore the coning is larger for the maneuver flight than the ballistic flight.

The scalloped features in the VAPP-8 angular motion of figure 13b are due to the trim moments and control mechanism induced yawing motions which both occur at the roll frequency. Within this interval of the flight, the roll rate is between 10 and 12 Hz. By comparison, the yaw frequency is approximately 2.5 Hz. Thus, within a yaw cycle the control mechanism and trim moments perturb the angular motion at the roll rate to produce the scalloped shapes.

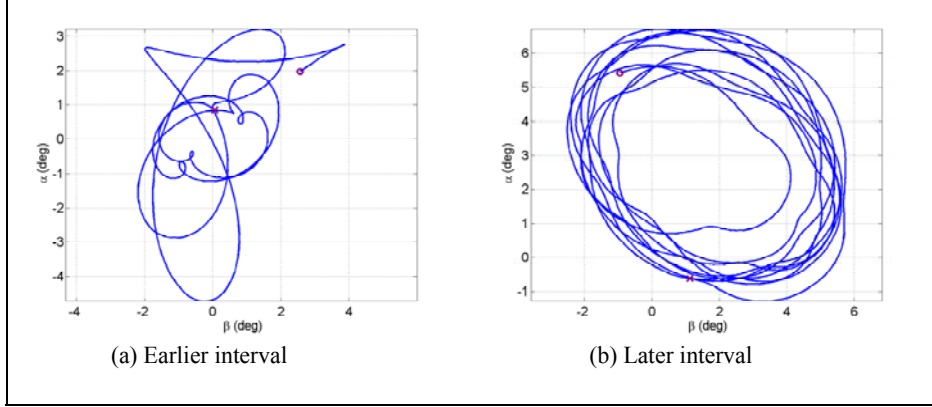


Figure 13. Reconstructed angular motion for VAPP-8.

#### 4.3 VAPP-7 and VAPP-8 Aerodynamic Coefficients

The aerodynamic coefficients derived for the 10-5mm airframe are shown in figures 14 and 15. Zero-yaw axial force coefficients ( $C_{x_0}$ ) for VAPP-8 and VAPP-7 agree well. The zero-yaw axial force coefficient increases slightly as Mach number increases.

The pitching moment coefficient was separated into the plane of the airframe containing the body and fins ( $C_{m_\alpha}$ ) and the plane containing the body, fins, and canards ( $C_{n_\beta}$ ). The difference between  $C_{m_\alpha}$  and  $C_{n_\beta}$  quantifies the degree of asymmetry in the airframe. An asymmetric pitching moment coefficient was obtained for VAPP-8 and the earlier portion of the flight of VAPP-7. As expected,  $C_{m_\alpha}$  was larger than  $C_{n_\beta}$  since the absence of canards moves the CP rearward. Near a Mach number of 0.85, the  $C_{n_\beta}$  for VAPP-8 and VAPP-7 agree better than the  $C_{m_\alpha}$  for VAPP-8 and VAPP-7. Perhaps nonlinearities with respect to angle-of-attack are not being captured or this experimental aerodynamic characterization is beyond the fidelity of the present data.

Adding the asymmetry into the analysis for the later phase of VAPP-7 did not improve the fit. Therefore, the average value for the two planes was used for the pitching moment coefficient at these Mach numbers (e.g., VAPP-7  $C_{m_\alpha}$  curve near Mach 0.7 in figure 14b). This averaging is supported by the data in figure 14b, where the averaged pitching moment coefficient for VAPP-7 lies between the results for  $C_{m_\alpha}$  and  $C_{n_\beta}$  for VAPP-8.

The pitch damping coefficient ( $C_{m_q} + C_{m_\alpha}$ ) in figure 14c and static side moment coefficient ( $C_{n_\alpha}$ ) in figure 14d contribute to the dynamic stability. Less pitch damping, for example, may be traded for a lower magnitude static side moment. This highlights the ambiguities sometimes associated with a particular aerodynamics characterization technique and provides support for the argument that employing multiple techniques can be required for the best overall aerodynamic assessment. These coefficients may also feature asymmetries, depending on roll orientation; however, such an effect was not significant in this situation.

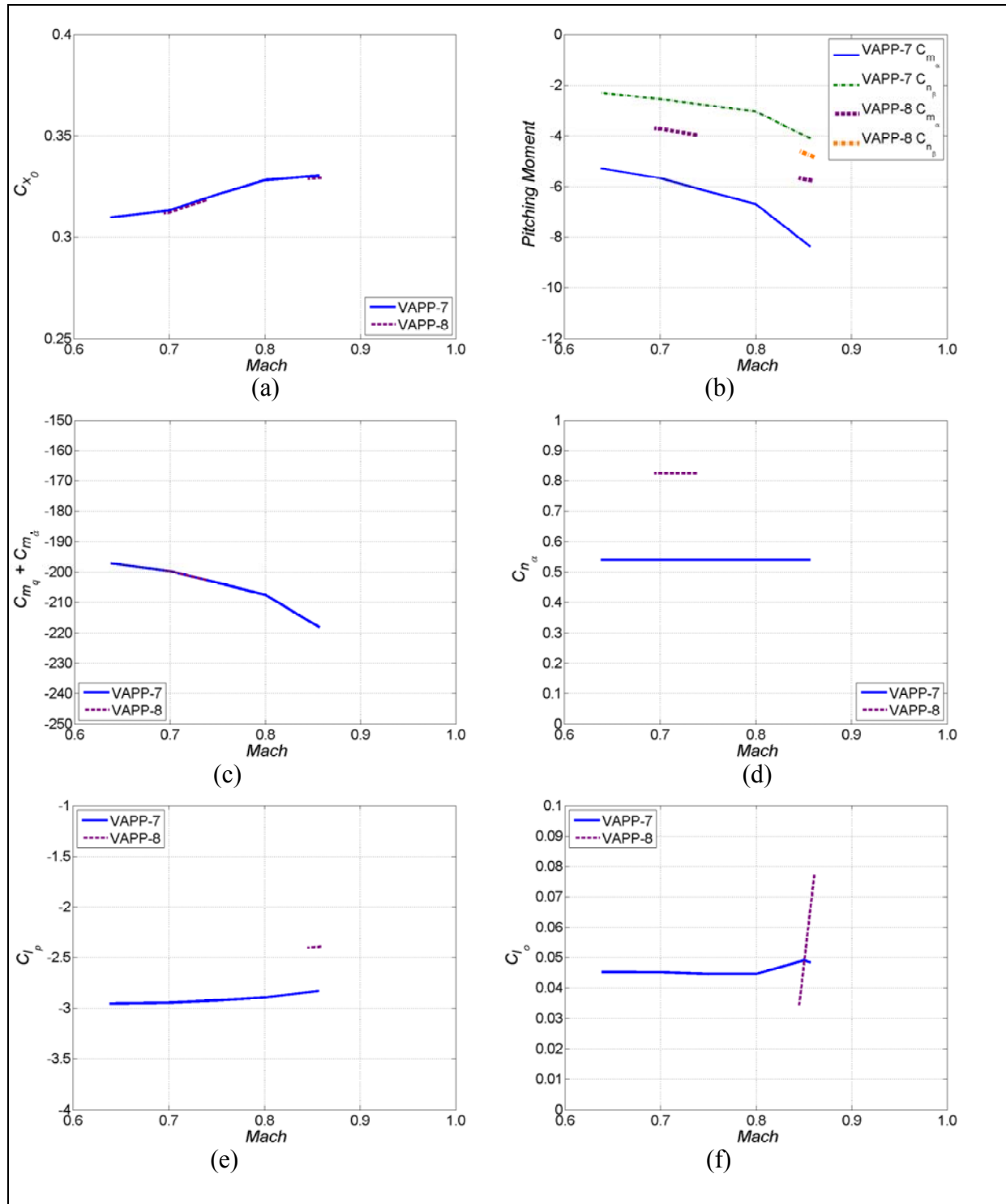


Figure 14. Aerodynamic coefficients for the 105-mm airframe.

The roll damping moment coefficient ( $C_{l_p}$ ) and static roll moment coefficient ( $C_{l_o}$ ) are shown in figures 14e and 14f. The dynamic roll moment coefficients of VAPP-7 and VAPP-8 agree to within experimental uncertainty. A large variation in static roll moment coefficient with Mach number near 0.85 for VAPP-7 may be unreliable given the static roll moment coefficient and roll rate history fit for VAPP-8.

Further aerodynamic data for the 105-mm projectile, not typically available from ballistic flights, are presented in figure 15. The normal force coefficient ( $C_{N_a}$ ) in figure 15a shows an increase of about 20% as Mach number increased from 0.65 to 0.85. An asymmetric normal force coefficient (i.e., different between the body-fin and body-fin-canard planes) was not obtained potentially since the normal force of the canards does not produce a motion which is readily observable in the measurements. The normal force coefficient, therefore, is averaged over roll.

Canard normal force coefficient (for both blades) and longitudinal CP location are provided in figures 15b and 15c. Comparison of the canard normal force coefficient with the normal force coefficient in figure 15a shows that the canards contribute about 20% of the normal force of the body and fins combined. The CP is located near the canard axis and moves slightly rearward as Mach number increases.

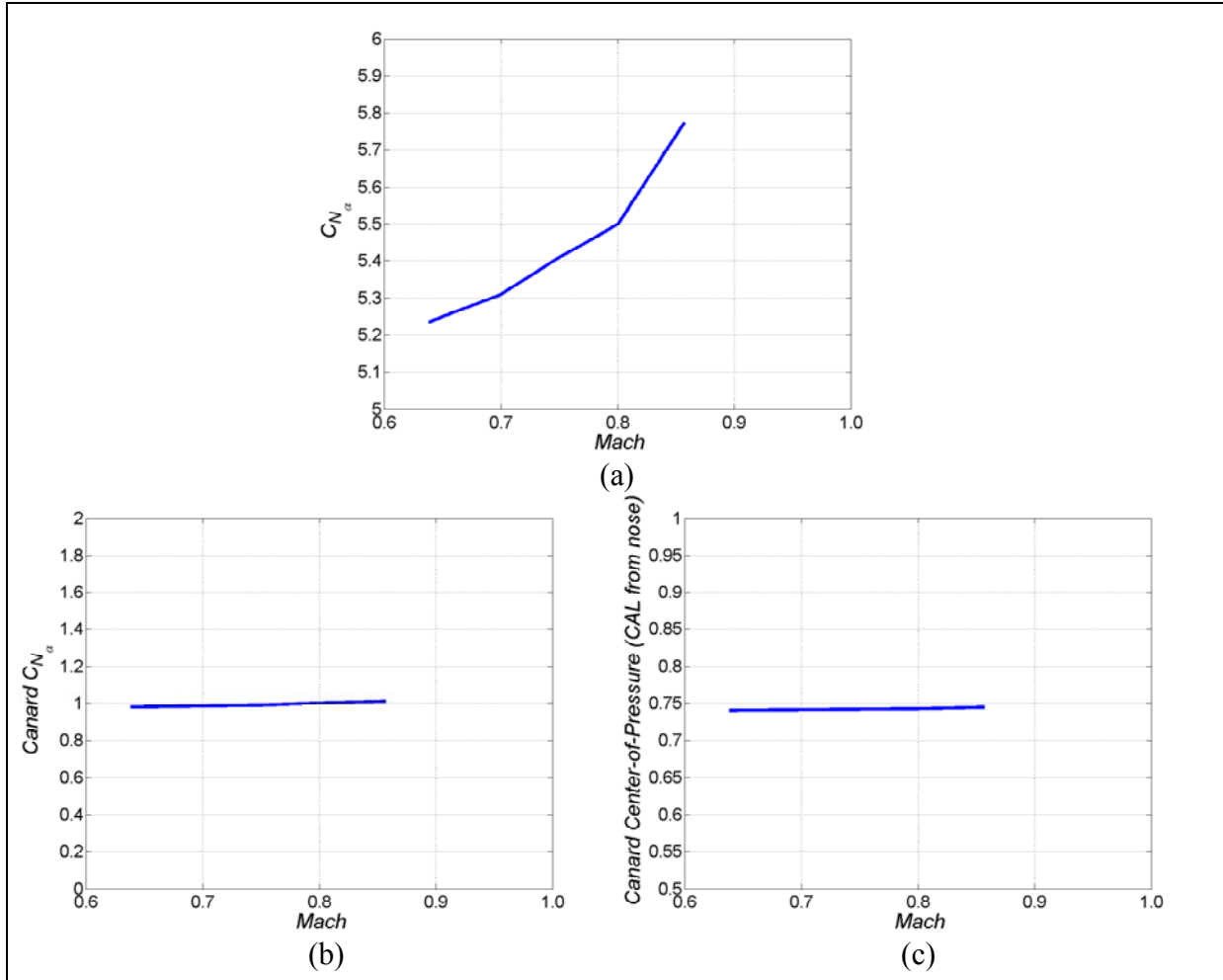


Figure 15. More aerodynamic coefficients for the 105-mm airframe (VAPP-8).

#### 4.4 The 120-mm Flight Dynamics: VAPP-13

The next projectile investigated was a 120-mm mortar round, VAPP-13. Radar and magnetometer data were obtained during the ballistic flight of VAPP-13. This projectile featured high static stability which contributed to there being only small angular motion during most of its flight. Appreciable angular motion was only encountered near the gun.

Comparisons of experimental data with 6-DOF calculations are provided in figures 16 and 17. Experimental measurement uncertainties are evident in the scatter of the radar data of figure 16. The roll rate increase from 0 at the gun to over 7 Hz in less than 1 s is illustrated in figure 17a. Figure 17b shows damping of the launch disturbances to less than 1° within 1 s from launch.

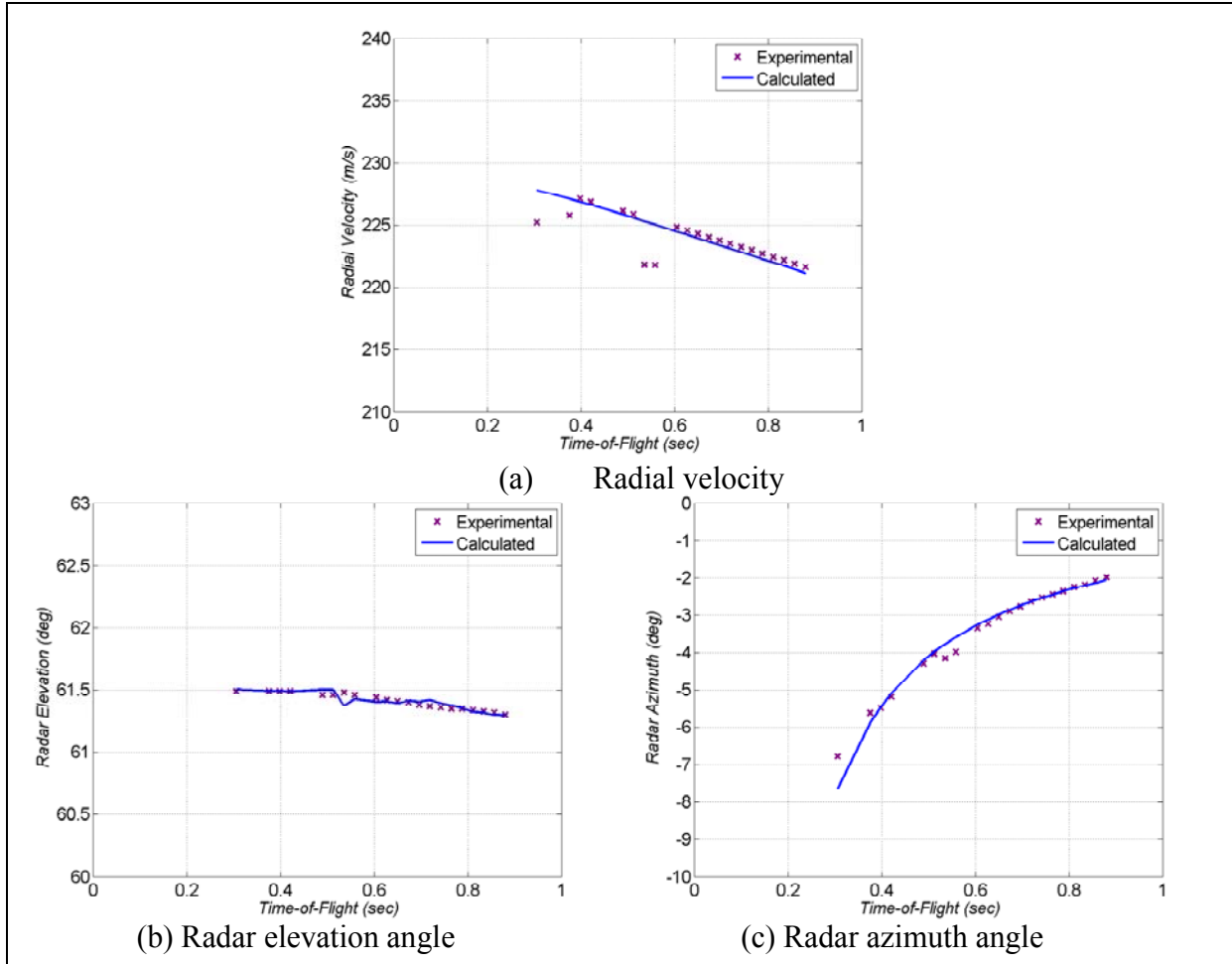


Figure 16. Experimental and calculated radar data for VAPP-13.

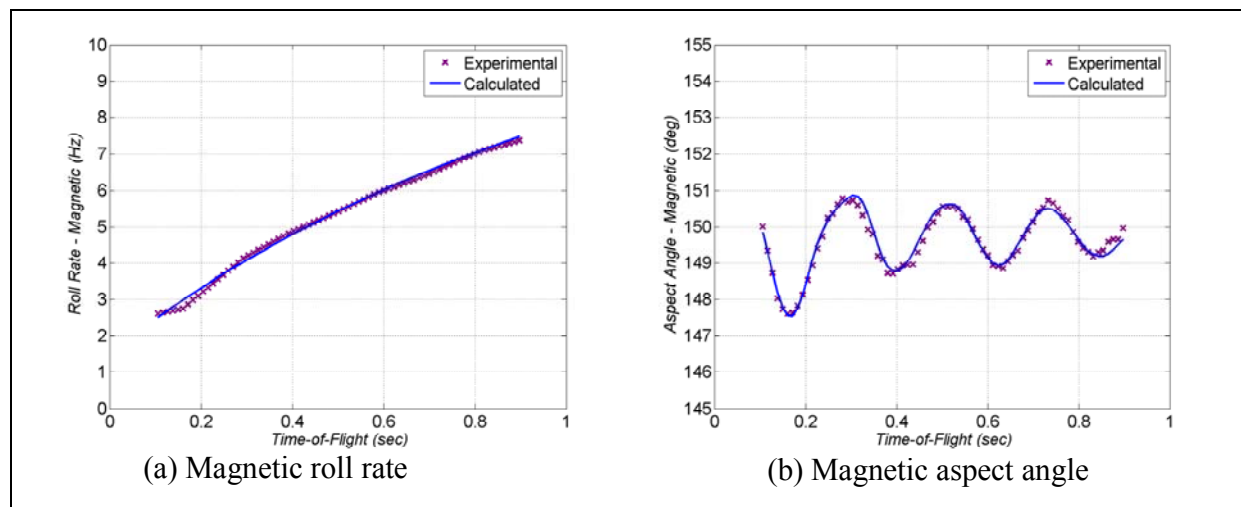


Figure 17. Experimental and calculated magnetic data for VAPP-13.

The reconstructed angular motion for VAPP-13 in figure 18 shows a maximum total angle-of-attack of about  $8^\circ$  resulting from an initial yawing rate that kicked the projectile nose up and to the right. Total angle-of-attack damped to less than  $1^\circ$  within 1 s.

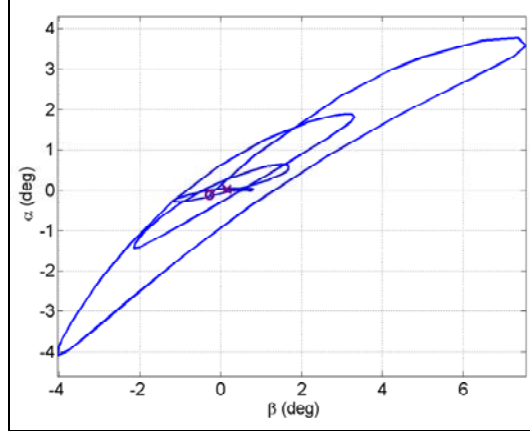


Figure 18. Reconstructed angular motion for VAPP-13.

#### 4.5 VAPP-13 Aerodynamic Coefficients

The aerodynamic coefficients for this 120-mm mortar configuration resulting from the parameter identification process are provided in figure 19. A limited Mach regime, between 0.65 and 0.7, was available for analysis due to the low amplitude angle-of-attack history during flight. The zero-yaw axial force, pitching moment, pitch damping moment, dynamic roll moment, and static roll moment coefficients do not change appreciably over this Mach range. The asymmetric pitching moment was quantified. Figure 19b demonstrates the relative decrease in the pitching moment coefficient in the plane containing the canards by shifting the CP nose-ward and increasing the normal force. An  $\sim 10\%$  change is evident between the pitching moment coefficients in the two planes; this physically agrees with a consideration of the relative size of canards and fins and location with respect to the CG.

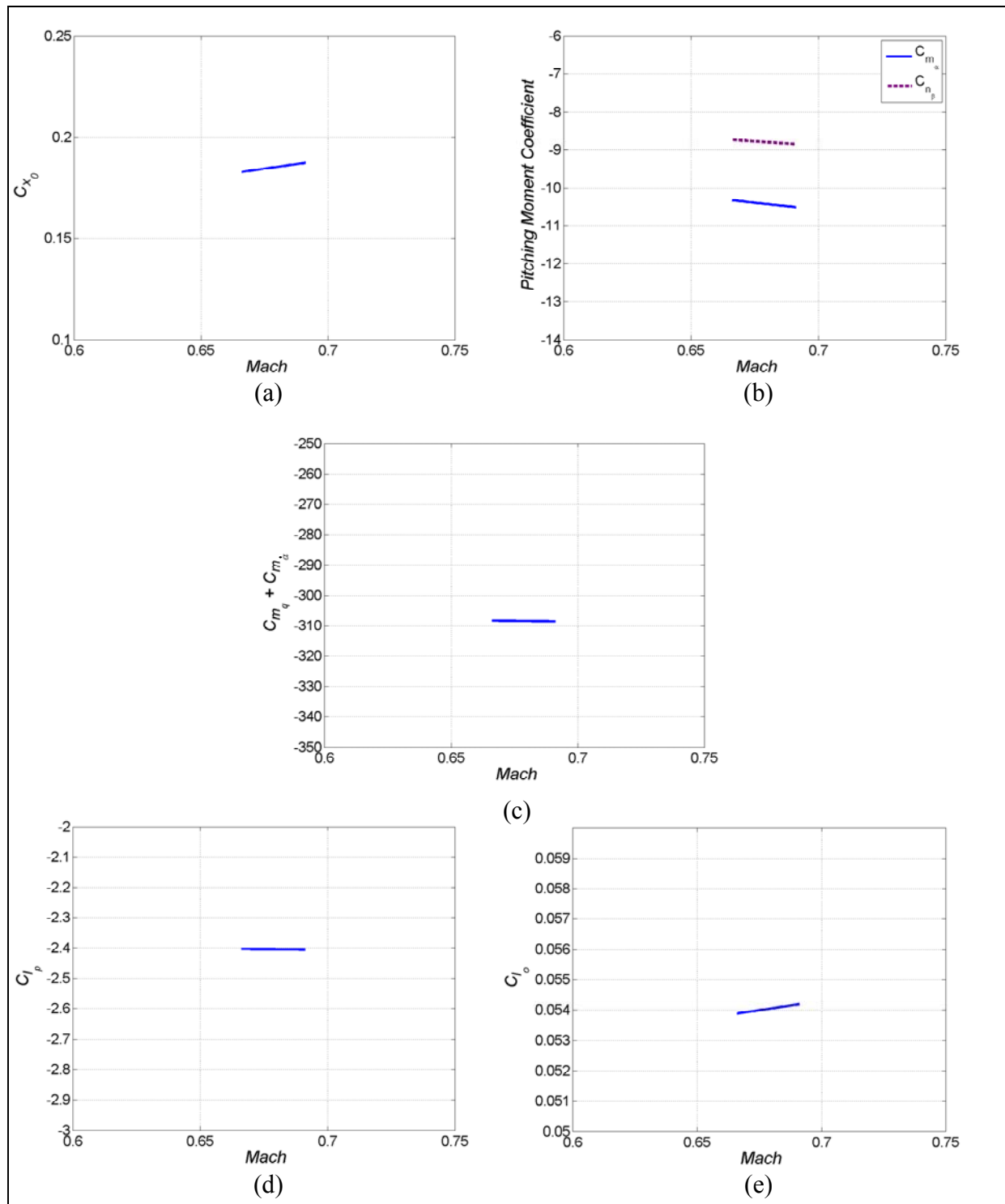


Figure 19. Aerodynamic coefficients for 120-mm airframe.

## 4.6 The 155-mm Flight Dynamics: VAPP-23

The remaining experimental aerodynamic characterizations to be discussed are for the flights of three identical, non-maneuvering, 155-mm artillery projectiles. For the first two shots (VAPP-23 and VAPP-24), radar, solar, accelerometer, and magnetic data were collected. For the third shot (VAPP-25), radar, solar, and accelerometer data were collected. All three rounds spanned supersonic to subsonic speeds.

For the VAPP-23 flight, analyses were performed using data from an approximately 8 s subsonic portion of the flight. Good agreement was achieved between all the calculated and experimental data within this interval. Calculated and experimental radar data are shown in figure 20.

Corresponding calculated and experimental roll rate data as estimated with the accelerometer ring are shown in figure 21a. The constant amplitude angular motion seen in the solar aspect angle and magnetic aspect angle data presented in figures 21b and c evidences a slight dynamic instability for the low angles of attack within this time interval. The direction of the coning motion was unambiguous because both solar and magnetic aspect angles were available.

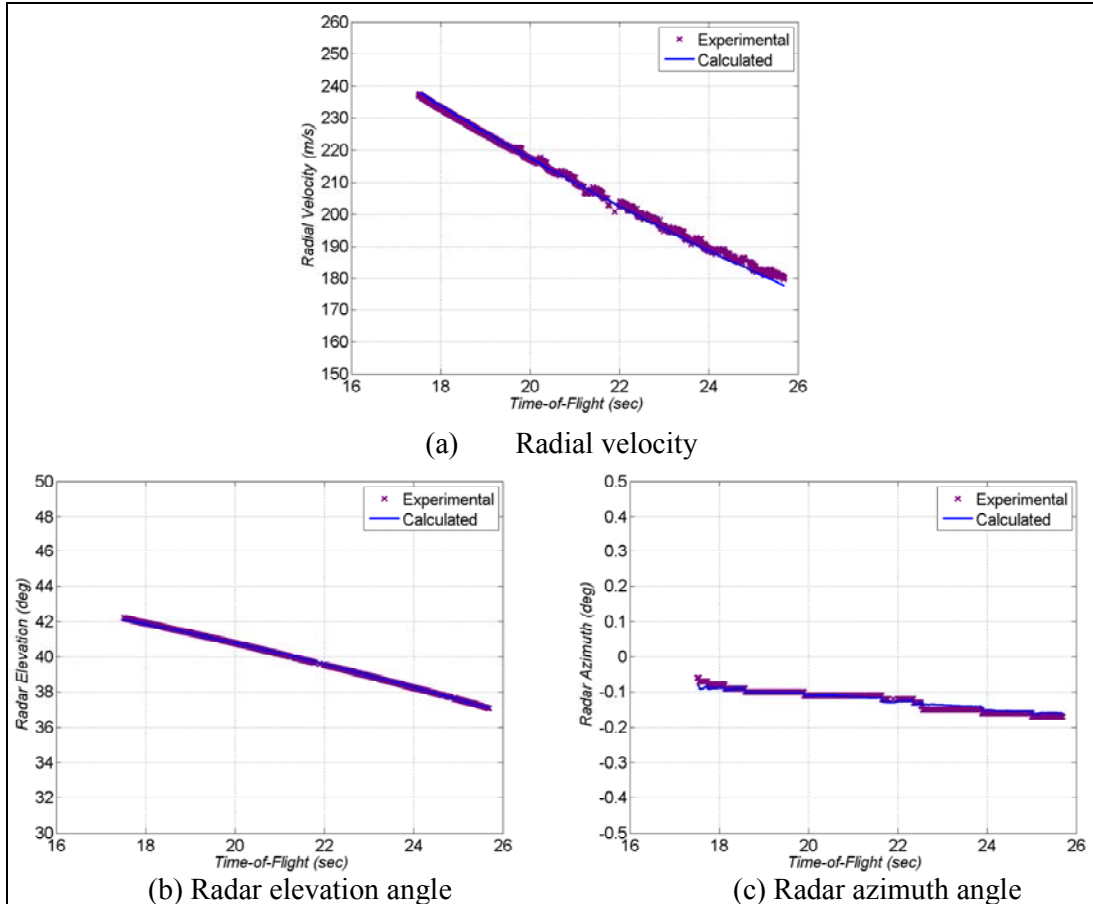


Figure 20. Experimental and calculated radar data for VAPP-23.

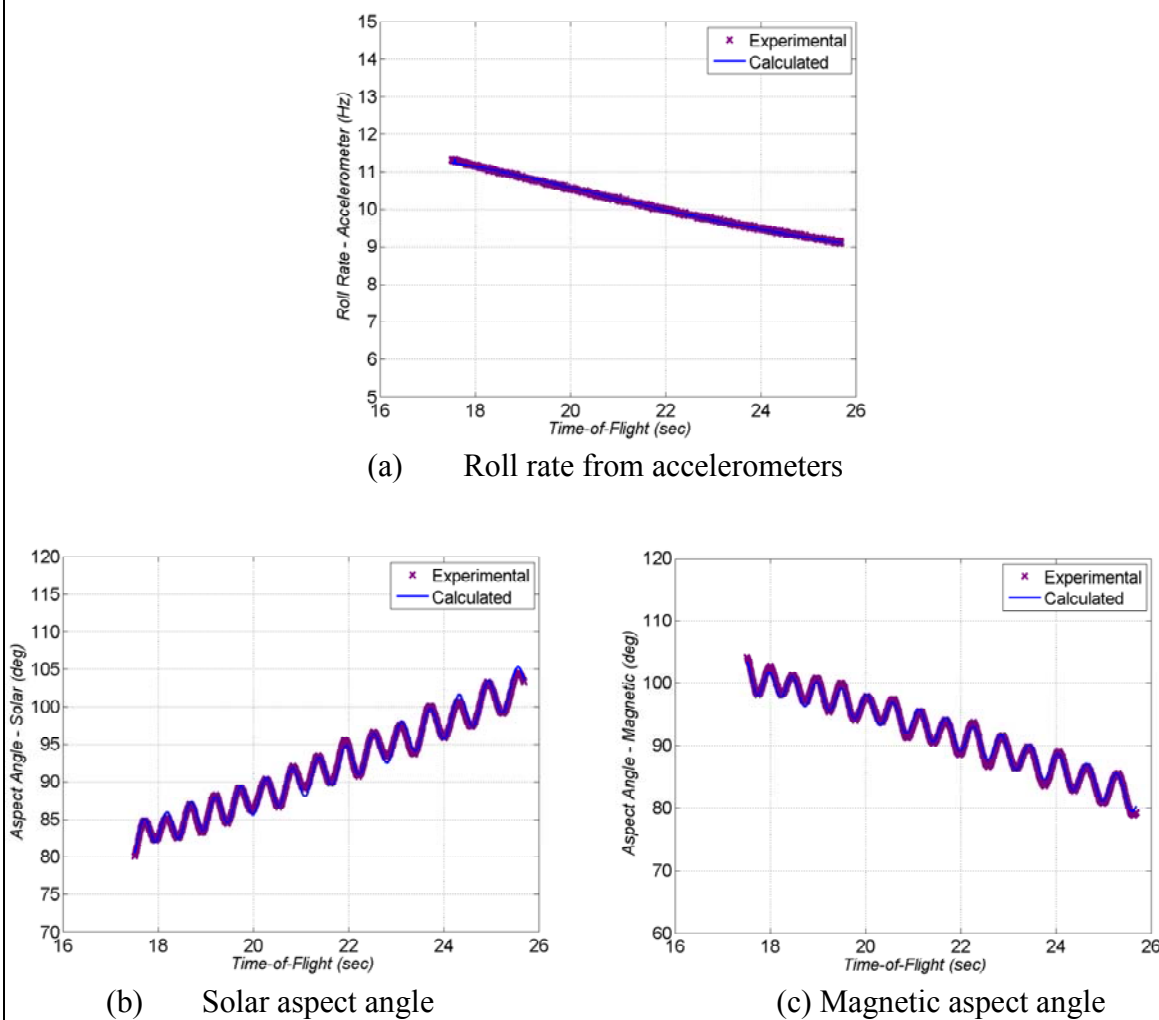


Figure 21. Experimental and calculated accelerometer, solar, and magnetic data for VAPP-23.

A positive static side moment coefficient was used to quantify the aerodynamic phenomenon producing this coning motion. This choice was supported by limited wind tunnel data. The resulting pitch-yaw plane motion due to the action of the static side moment can be seen in figure 22. The clockwise coning motion has a magnitude of between  $2^\circ$  and  $2.5^\circ$ .

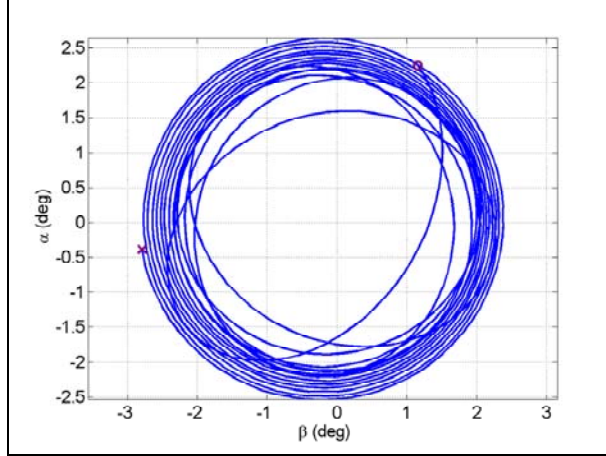


Figure 22. Reconstructed angular motion for VAPP-23.

#### 4.7 The 155-mm Flight Dynamics: VAPP-24

VAPP-24 was identical in configuration to VAPP-23. Two intervals of the flight data from VAPP-24 were used for the analysis. The Mach regime of VAPP-24 ranged from supersonic to transonic during the first interval and was wholly subsonic during the second interval. Fits to the radar data for both intervals are presented in figure 23. Radar matches and all other fit metrics fell within the bounds provided in table 3.

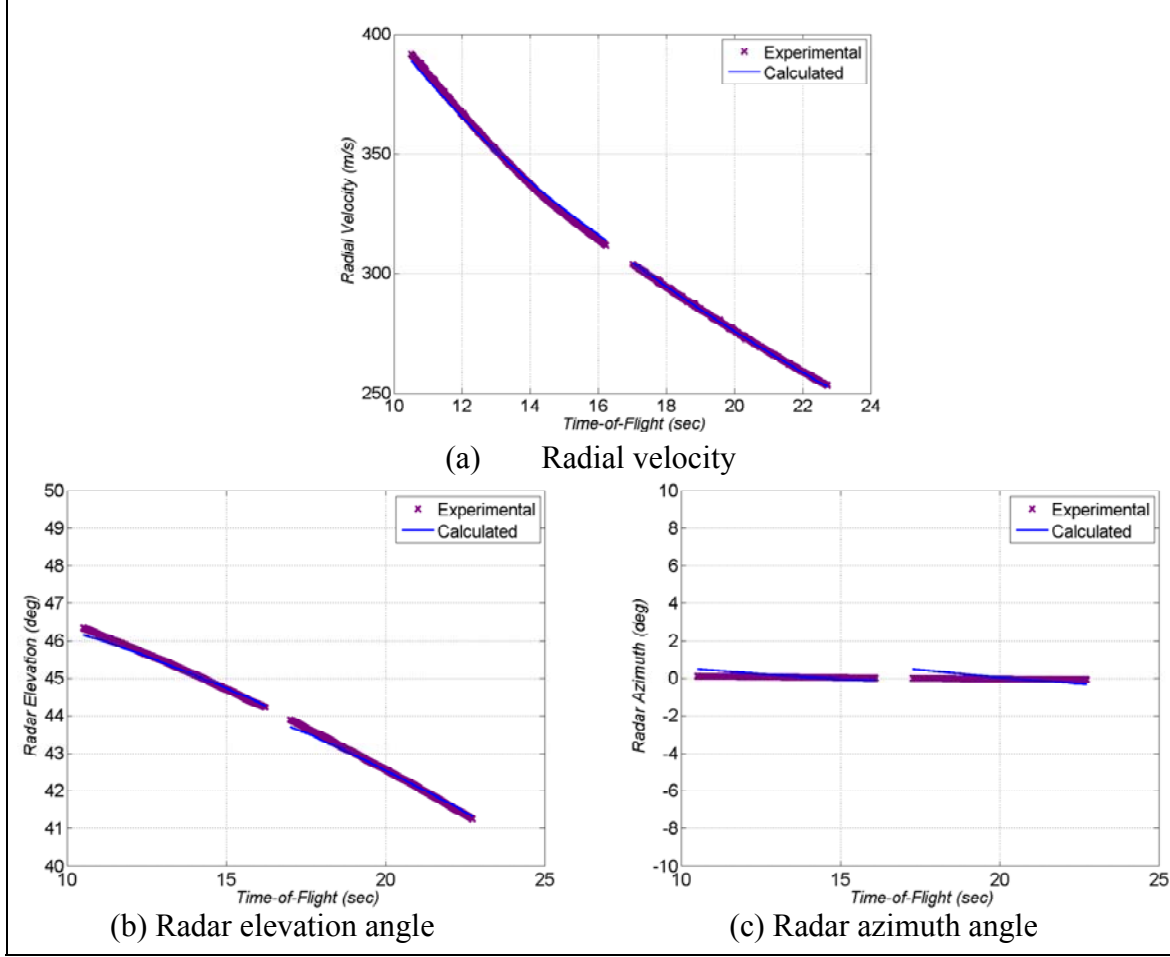


Figure 23. Experimental and calculated radar data for VAPP-24.

The calculated roll rate in figure 24a matches the experimental data better for the later phase of flight than the earlier phase. Consequently, estimated static and dynamic roll moment coefficients in the lower Mach regime should have greater accuracy.

Satisfactory agreement was achieved between the calculated and experimental data for the solar and magnetic aspect angles during both intervals. As solar and magnetic aspect angle histories were available and distinct, the direction of coning motion was determined using this analysis methodology and an independent approach (POINTER) and relative magnitude information about the side moments was obtained. VAPP-24 underwent a reversal in coning direction in mid-flight. In the first interval, while at supersonic through transonic speeds, coning was counterclockwise and a negative dynamic side moment achieved the required match to the solar and magnetic aspect angles. Later in flight, when VAPP-24 was subsonic, coning was clockwise and the match to experimental data was obtained with a positive static side moment. While limited wind tunnel data supports use of a static side moment for matching the angular motion history when at subsonic speeds, further investigation (e.g., CFD) must be performed to further quantify the static and dynamic side moment coefficients for this projectile.

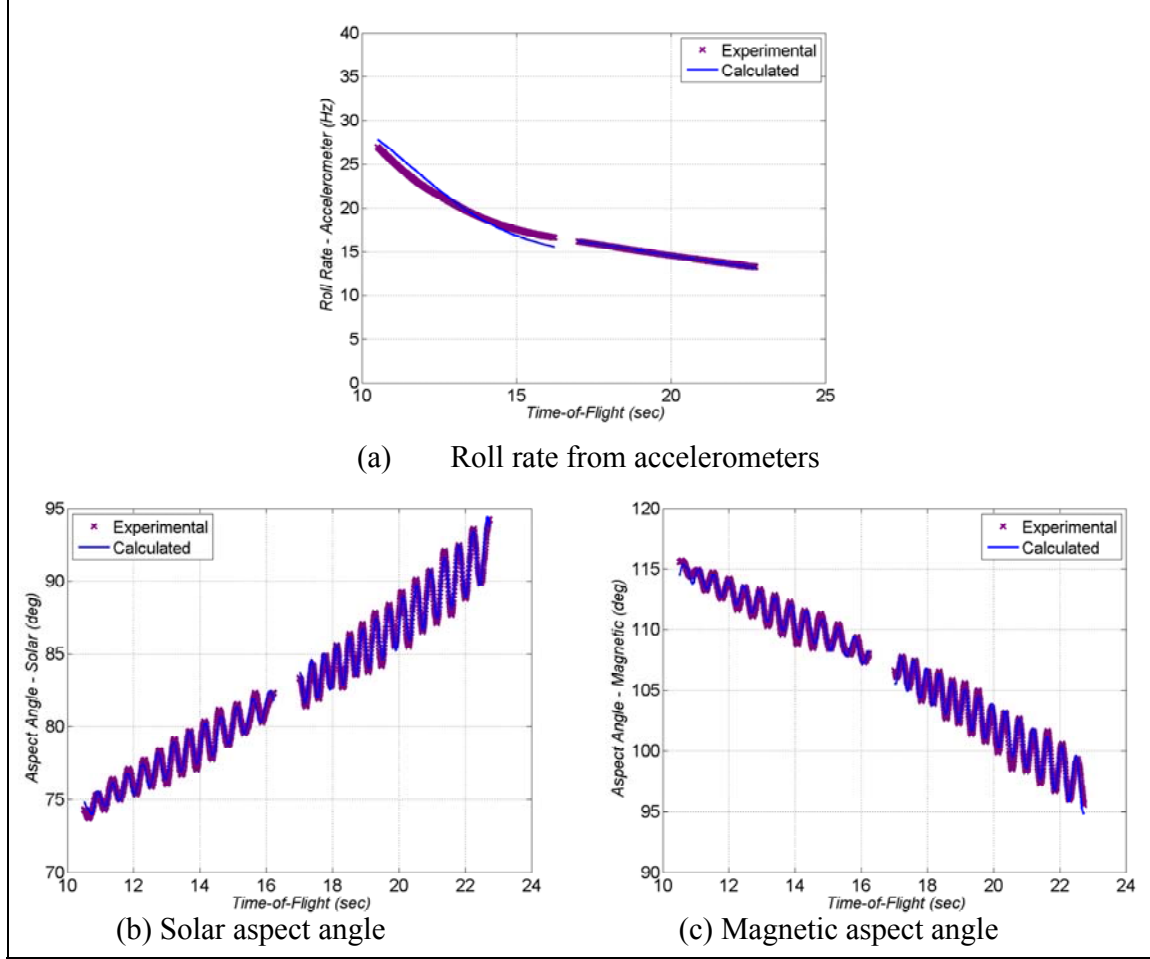


Figure 24. Experimental and calculated accelerometer, solar, and magnetic data for VAPP-24.

The angular motion reconstruction plots for the two intervals are given in figure 25. Proceeding along the respective curves, the coning during the first interval (figure 25a) is in the counter-clockwise direction with about  $1^\circ$  amplitude. For the later, subsonic interval, figure 25b shows an approximate  $2^\circ$  coning magnitude with a clockwise sense. An angular motion history for the entire trajectory was independently estimated using the POINTER methodology. These estimates agreed with the angular reconstructions shown here in both direction and magnitude.

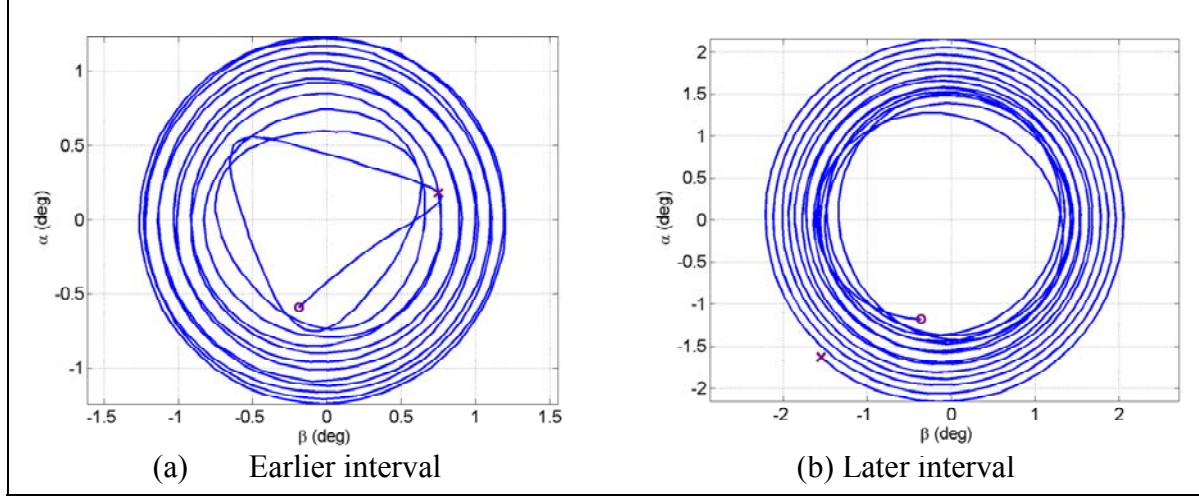


Figure 25. Reconstructed angular motion for VAPP-24.

#### 4.8 The 155-mm Flight Dynamics: VAPP-25

For the final 155-mm projectile flight, VAPP-25, radar, accelerometer, and solar data were obtained. A portion of these data during the supersonic to transonic Mach regimes was used for processing. Figure 26 demonstrates that sufficient agreement between the measured and calculated radar data was accomplished.

The experimental solar aspect angle data in figure 27b show a growth of angle of attack during this interval. Recalling the analysis of VAPP-24 indicated that the observed instability at these speeds was likely attributable to a negative dynamic side moment, this parameter was chosen for fitting the VAPP-25 solar data. Non-linearity in the dynamic side moment was able to be quantified since the measured total angle-of-attack was higher for VAPP-25 than VAPP-24.

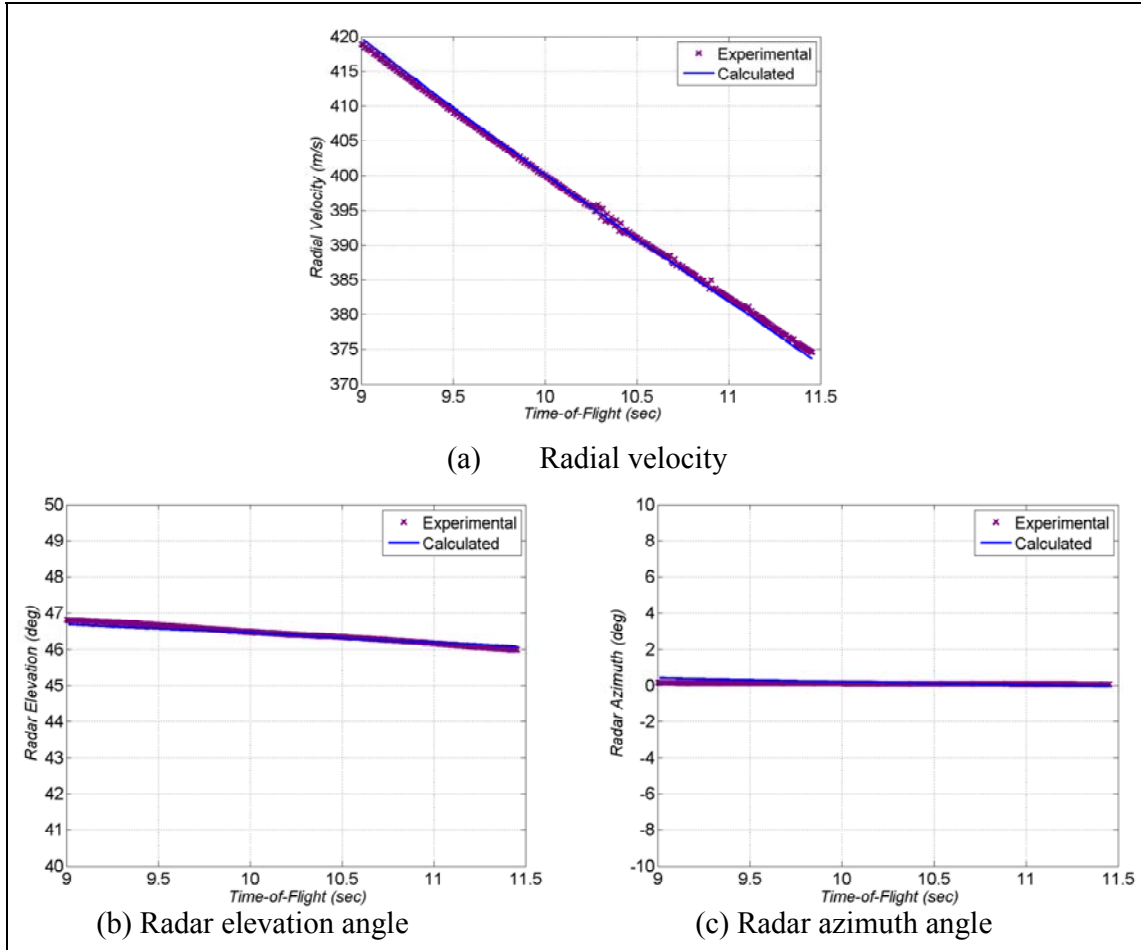


Figure 26. Experimental and calculated radar data for VAPP-25.

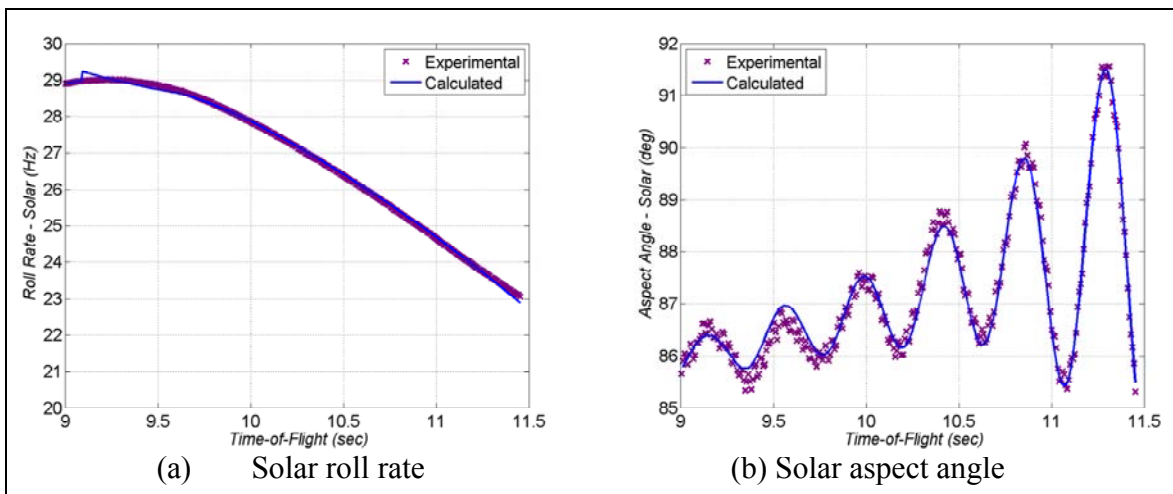


Figure 27. Experimental and calculated accelerometer and solar data for VAPP-25.

The resulting reconstructed angular motion is shown in figure 28. The angle-of-attack magnitude grows to almost  $4^\circ$  by the end of the evaluated portion of flight. The direction of the spiral, in accordance with a negative dynamic side moment, is counter-clockwise.

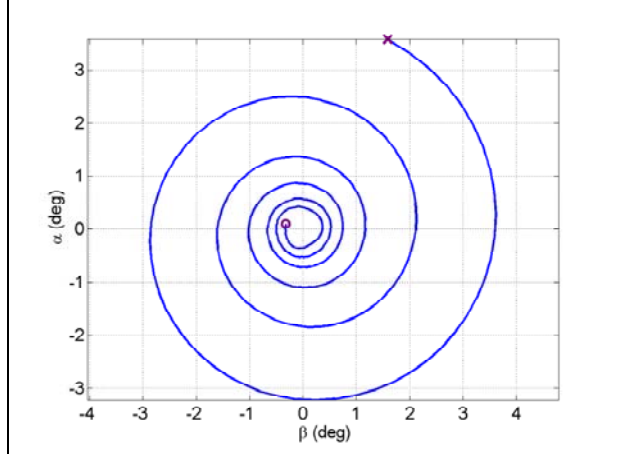


Figure 28. Reconstructed angular motion for VAPP-25.

#### 4.9 VAPP-23, 24, and 25 Aerodynamic Coefficients

The aerodynamic coefficients for the 155-mm airframe, compiled from analysis of the flights of VAPP-23, VAPP-24, and VAPP-25, are provided in figures 29 and 30. The flight data obtained estimate of zero-yaw axial force coefficient (figure 29a) shows some scatter. More analysis could perhaps refine these estimates; however, the zero-yaw axial force coefficients provided in figure 29a were hand-faired and ultimately used in the development of a GNC system that produced successful guide-to-hit flight experiments.

The pitching moment coefficients are given in figure 29b. The asymmetric pitching moment was unable to be determined; possibly due to a small difference in pitching moments between the canard and non-canard plane for this projectile. Thus, the pitching moment coefficients likely represent a roll-average.

Pitch damping coefficients presented in figure 29c illustrate an approximately 20% increase in pitch damping through the transonic regime. The positive static side moment coefficient that was determined during subsonic flight is given in figure 29d. More discussion of the pitch damping and static side moment is provided next during explanation of the dynamic instability of the 155-mm projectile.

The dynamic and static roll moment coefficients are shown in figures 29e and 25f, respectively. Slip band obturators were used for the 155-mm rounds to produce low roll rates at launch. When the tailfins deployed, there was a rapid increase in spin for about the first 5 s of the flight of

VAPP-23 and about the first 9 s of the flight of VAPP-24 and VAPP-25. Thereafter, because tailfin shape is the mechanism for creating projectile spin, there is a direct correlation between speed and spin rate. All the analyses were for intervals with this direct correlation. Spin rates ranged from approximately 10–30 Hz within the analyzed data while corresponding speeds ranged from approximately 250–420 m/s. This behavior is reflected in the static roll moment coefficient increasing for Mach greater than one.

Out of eight total experimental flights of the 155-mm projectile (three of which, VAPP-23, VAPP-24, and VAPP-25 are analyzed in this effort), four flights maintained a  $2^{\circ}$ – $3^{\circ}$  magnitude yawing motion in the transonic Mach regime and four flights had a yawing magnitude which grew to over  $10^{\circ}$  in the transonic Mach regime. This intermittency is a characteristic that should be eliminated during the development of precision munitions. The control authority must increase to account for a bi-modal (shorter/high yaw impacts and longer/low yaw impacts) ballistic dispersion.

The intermittency of high yaw growth was reproduced through the introduction of a negative dynamic side moment that is non-linear with angle-of-attack. The dynamic side moment coefficient obtained from the flights of VAPP-24 and VAPP-25 is shown in figure 30. Total angle-of-attack near  $2^{\circ}$  appeared to be the threshold angle-of-attack for instability since the magnitude of the dynamic side moment increased by a factor of 2. At angles-of-attack higher than  $2^{\circ}$ , the magnitude of the dynamic side moment reduced. It is unknown if the underlying phenomenon producing this instability is due to flow interactions between the body, fins and canards, or some other mechanism.

It is presumed that minor variations in angle-of-attack in the transonic Mach regime due to atmospheric effects (e.g., wind) or projectile asymmetries (e.g., mass imbalance or external shape) dictate the degree of instability encountered in the individual experimental flights since the dynamic side moment scales as the total angle-of-attack.

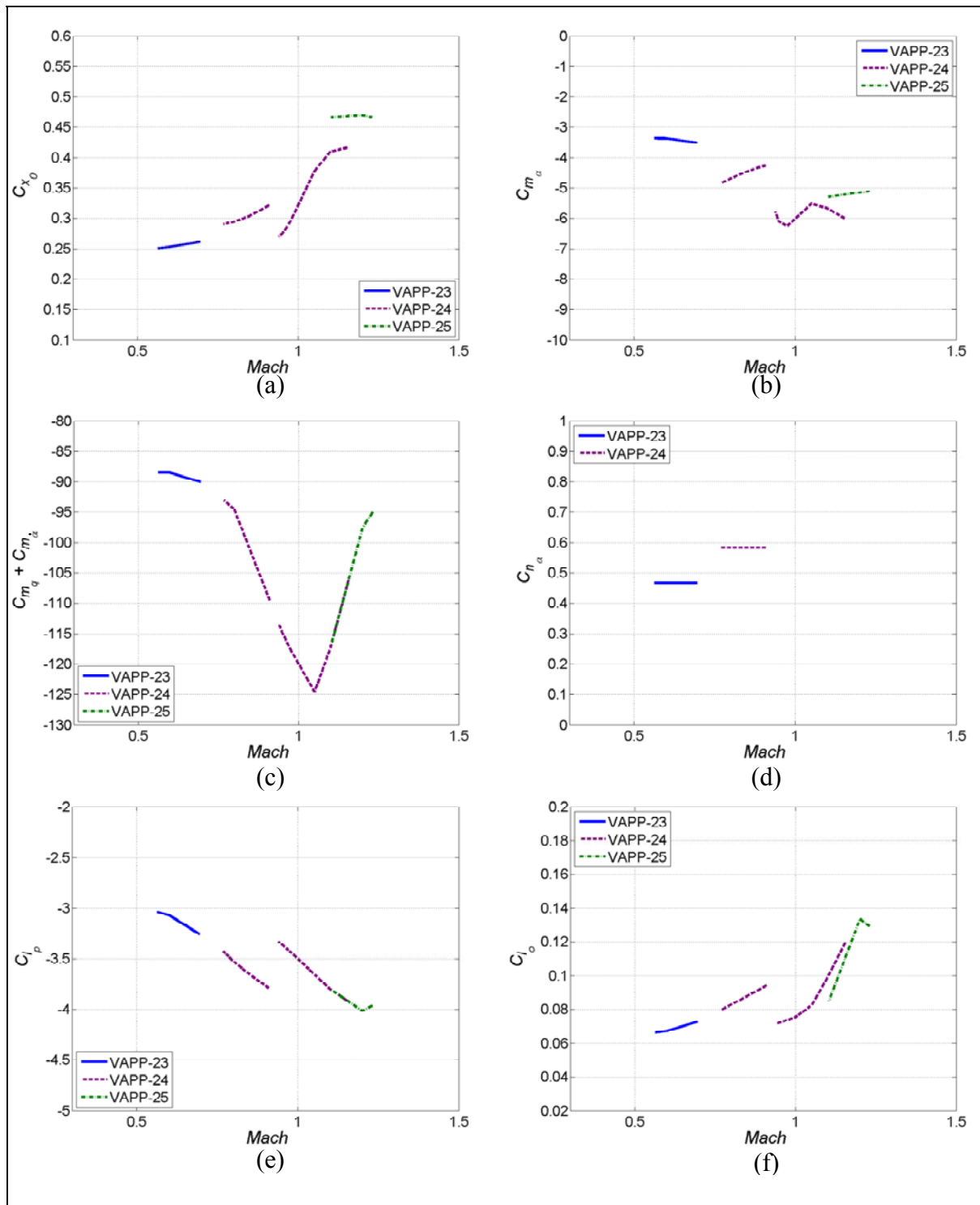


Figure 29. Aerodynamic coefficients for 155-mm airframe.

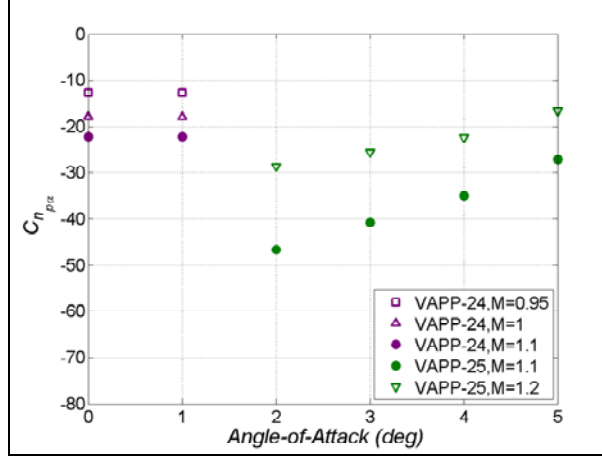


Figure 30. Dynamic side moment coefficient for 155-mm airframe.

#### 4.10 Dynamic Stability of 155-mm Projectile

The 155-mm projectile featured a strong transonic instability and also reversed coning direction in mid-flight. An analysis of the dynamic stability of this projectile was undertaken using this aerodynamic characterization and projectile linear theory (14) to better understand these phenomena.

In projectile linear theory, equations of motion for the pitch and yaw angle-of-attack have a closed-form solution. This solution takes the form of a damped sinusoid. The period of the sinusoid is dictated by the yawing rate of the airframe. An exponential term (exponential raised to a power denoted as the damping rate) prescribes the change in amplitude of this sinusoid. Positive damping rates result in an increase in the amplitude of the angle-of-attack and negative damping rates decrease angle-of-attack amplitude.

Furthermore, the angular motion solution is often separated into two modes: fast (or nutation) and slow (or precession). A damping rate and yawing rate is associated with each mode in linear theory. This formulation is useful in that it enables the type of instability (fast mode or slow mode) to be identified along with the underlying cause (e.g., static side moment, dynamic side moment, pitch damping).

The analysis of the flight of VAPP-24 indicated that a reversal in the coning direction occurs in mid-flight. This behavior was due to different dynamic flight instabilities in separate Mach regimes. To illustrate these dynamic instabilities, the damping rates and yawing rates were calculated for subsonic (Mach = 0.75) and transonic (Mach = 1.1) flight using projectile linear theory and are given in figure 31. An angle-of-attack averaged dynamic side moment was used in these calculations to permit insight into the phenomena at different Mach number.

Inspection of the damping rates in figure 31a show a strongly damped slow mode and a weakly damped fast mode at Mach 0.75. The static side moment is the main contributor in producing the weakly damped fast mode. At transonic speeds, these trends flip to some degree; the slow mode is undamped and the fast mode is strongly damped. The undamped slow mode is produced by the dynamic side moment. Reducing the fin cant, and therefore the roll rate, would increase the damping rate of the slow mode; however, roll-yaw resonance would be an issue if roll rate were reduced further. Thus, this projectile has a potentially minor fast mode instability due to a static side moment for subsonic mach numbers and a strong slow mode instability due to a dynamic side moment at transonic mach numbers.

The yawing rates for the fast and slow mode are presented in figure 31b, along with the steady state roll rate determined from projectile linear theory. For slowly rolling fin-stabilized projectiles, the fast and slow mode yawing rates are nearly equal magnitude with opposite sign. Comparing the fast mode yawing rate with the roll rate shows a separation sufficient to avoid roll-yaw resonance.

The data in figure 31b illustrate that the fast mode yawing is in the same direction as the roll rate. Thus, for right-hand rolling projectiles, the fast mode is also yawing in a clockwise direction when viewed from behind the projectile. Alternatively, the slow mode yawing is in a counter-clockwise direction. As an example, at Mach number 1.1, the projectile is rolling at 20 Hz in the clockwise direction, the fast mode is yawing (if excited) at 5 Hz in the clockwise direction, and the slow mode is yawing (if excited) at about 4 Hz in the counter-clockwise direction.

Combining the information in figure 31 with the angular motion reconstructions in figures 22, 25, and 28 completes the dynamic stability analysis of this projectile. For the launch and flight conditions used here, at transonic Mach numbers a dynamic side moment (nonlinear with angle-of-attack) produces yaw growth with coning motion in the counter-clockwise direction (see figures 25a and 28). As Mach number decreases in flight to subsonic, a weak fast mode instability due to a static side moment appears. This causes the projectile to cease coning motion with counter-clockwise sense and begin to cone in the clockwise direction with a magnitude near  $2^\circ$  (see figures 22 and 25b). This dynamic stability analysis is based on the magnitude of the static (figure 29d) and dynamic side moment (figure 30) coefficients obtained in these experiments; further analysis should be performed to refine these data.

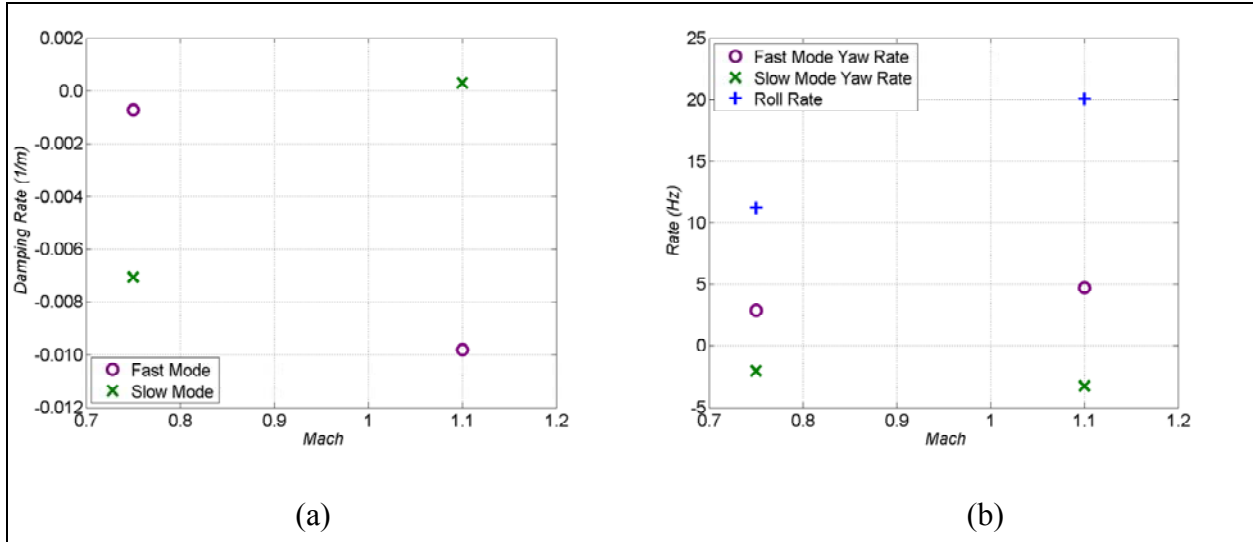


Figure 31. Dynamic instability metrics for 155-mm airframe.

## 5. Conclusions

This effort fully characterized the aerodynamics of precision munitions, including asymmetries, static side moments, nonlinear dynamic side moments, normal forces, and the control mechanism terms for the first time from elevated gun firings. These results enable 6-DOF simulation, analysis of dynamic flight stability, and projectile design.

Maneuverability, roll rate, and dynamic stability were critical parameters for these precision munitions. The 105-mm projectile met all three performance objectives. VAPP-8 demonstrated an approximately 30% extension in range from the ballistic flight due to the canard deflections. The control-induced angle-of-attack during glide was approximately  $3^\circ$ . The roll rate of this 105-mm projectile was sufficiently higher than the yaw rate so that roll-yaw resonance was avoided. The roll rate was satisfactory for roll angle estimation and CAS bandwidth, both requirements of the GNC system. A weak dynamic instability (coning motion of  $1^\circ$ – $3^\circ$ ) for the 105-mm projectile was not detrimental to the overall system effectiveness.

The 120-mm airframe was less successful at meeting all design objectives. Maneuverability was inadequate due to the high static stability. Roll rate was satisfactory for resonance and GNC purposes. Negligible coning motion was observed during flights of the 120-mm mortar. Dynamic stability was enhanced by the high static stability. Future airframe modifications for the 120-mm mortar should focus on reducing the effectiveness of the tailfins (thereby reducing static stability) while preserving the roll rate.

The 155-mm projectile met maneuverability and roll rate objectives, but exhibited dynamic instabilities. The  $2^\circ$  coning motion at subsonic velocities was acceptable. In the transonic Mach regime, however, the non-linear dynamic side moment was extremely sensitive to minor differences in the angle-of-attack. Angle-of-attack non-linearity and the roll rate at transonic speeds contributed to coning amplitudes greater than  $10^\circ$  in the flights. It was just as problematic that coning as low as  $2^\circ$  was also encountered in flights at transonic speeds. Further studies must determine the flow mechanisms which are responsible for this transonic instability. Modifications to the fin or canard configuration would likely mitigate of these effects.

This experimental characterization provided a fundamental understanding of the ballistic and maneuvering flights of these airframes. A variety of complex physical processes was observed and modeled, including a reversal in the direction of coning motion in mid-flight was detected. The dynamics which dictated this switching in the direction of coning were explained.

This analysis impacted programs by providing a high quantity of actual flight-based aerodynamic and flight dynamic information with less costly and time-consuming testing. Ultimately, these results enabled successful guide-to-hit flight experiments on multiple projectile calibers.

A limitation to these techniques is that the full range of Mach in the flights cannot be exploited for aerodynamics because all states of the projectile dynamics are not being excited. Future efforts will focus on both means to persistently excite the projectile in flight and methods to obtain aerodynamics at lower excitation amplitude. Additionally, methods to reduce the analysis time would be beneficial.

---

## 6. References

---

1. Fresconi, F.; Brown, T.; Celmins, I.; DeSpirito, J.; Ilg, M.; Maley, J.; Magnotti, P.; Scanlan, A.; Stout, C.; Vazquez, E. Very Affordable Precision Projectile System and Flight Experiments. Presented at the 27<sup>th</sup> Army Science Conference, Orlando, FL, 2010.
2. Davis, B.; Guidos, B.; Harkins, T. *Complementary Roles of Spark Range and Onboard Free-Flight Measurements for Projectile Development*; ARL-TR-4910; U.S. Army Research Laboratory: Aberdeen Proving Ground, MD, August 2009.
3. Chapman, G.; Kirk, D. A New Method for Extracting Aerodynamic Coefficients from Free-Flight Data. *Amer. Inst. of Aeronautics and Astronautics Journ.* **1970**, 8 (4), 753–758.
4. Hathaway, W.; Whyte, R. *Aeroballistic Research Facility Free Flight Data Analysis Using the Maximum Likelihood Method*; AFATL-TR-79-98; U.S. Air Force Armament Laboratory: Eglin Air Force Base, FL, December 1979.
5. Davis, B.; Hathaway, W.; Hathaway, A.; Thompson, A. *Extending Telemetry Reduction to Aerodynamic Coefficients and Trajectory Reconstruction (EXTRACTR) Flight Experiment Using 155-mm M483A1 Projectiles*; ARL-TR-3563; U.S. Army Research Laboratory: Aberdeen Proving Ground, MD, August 2005.
6. Fresconi, F.; Harkins, T. *Aerodynamics of a 120-mm Mortar with a Guidance Kit Obtained from Telemetry Experiments*; ARL-TR-4569; U.S. Army Research Laboratory: Aberdeen Proving Ground, MD, September 2008.
7. Trohanowsky, R.; Vazquez, E.; Duca, M. *Subsonic Wind Tunnel Test of 67% Scale 120mm VAPM – Very Affordable Precision Mortar*; AERO-WT-09-01; U.S. Army Armament Research, Development and Engineering Center: Picatinny Arsenal, NJ, March 2009.
8. Thompson, A. *Calibration of an Orthogonal Cluster of Magnetic Sensors*; ARL-TR-4868; U.S. Army Research Laboratory: Aberdeen Proving Ground, MD, July 2009.
9. Harkins, T.; Davis, B.; Brown, G.; Fresconi, F.; Hathaway, W.; Hathaway, A.; Lovas, A. *Observing Airframe States in Free-Flight Experimentation*; ARL-TR-4635; U.S. Army Research Laboratory: Aberdeen Proving Ground, MD, November 2008.
10. Harkins, T. *Understanding Body-Fixed Sensor Output From Projectile Flight Experiments*; ARL-TR-3029; U.S. Army Research Laboratory: Aberdeen Proving Ground, MD, September 2003.
11. Hepner, D.; Harkins, T. Method and System for Determining the Pointing Direction of a Body in Flight. U.S. Patent 6398155, June 2002.

12. Hepner, D.; Harkins, T. *Determining Inertial Orientation of a Spinning Body with Body-Fixed Sensors*; ARL-TR-2313; U.S. Army Research Laboratory: Aberdeen Proving Ground, MD, January 2001.
13. Harkins, T. *A Unique Solution for Flight Body Angular Histories*; ARL-TR-4312; U.S. Army Research Laboratory: Aberdeen Proving Ground, MD, November 2007.
14. Nicolaides, J. On Missile Flight Dynamics; Ph.D. Dissertation, Catholic University of America, 1963.

NO. OF  
COPIES ORGANIZATION

1 DEFENSE TECHNICAL  
(PDF INFORMATION CTR  
only) DTIC OCA  
8725 JOHN J KINGMAN RD  
STE 0944  
FORT BELVOIR VA 22060-6218

1 DIRECTOR  
US ARMY RESEARCH LAB  
IMNE ALC HRR  
2800 POWDER MILL RD  
ADELPHI MD 20783-1197

1 DIRECTOR  
US ARMY RESEARCH LAB  
RDRL CIM L  
2800 POWDER MILL RD  
ADELPHI MD 20783-1197

1 DIRECTOR  
US ARMY RESEARCH LAB  
RDRL CIM P  
2800 POWDER MILL RD  
ADELPHI MD 20783-1197

1 DIRECTOR  
US ARMY RESEARCH LAB  
RDRL D  
2800 POWDER MILL RD  
ADELPHI MD 20783-1197

ABERDEEN PROVING GROUND

1 DIR USARL  
RDRL CIM G (BLDG 4600)

<u>NO. OF COPIES</u>	<u>ORGANIZATION</u>	<u>NO. OF COPIES</u>	<u>ORGANIZATION</u>
4	RDECOM ARDEC RDAR MEF E M HOLLIS A SANCHEZ R HOOKE J MURNANE BLDG 94 PICATINNY ARSENAL NJ 07806-5000	4	US ARMY TACOM ARDEC AMSRD AAR AEM A W KOENIG G MALEJKO T RECEHIA E VAZQUEZ PICATINNY ARSENAL NJ 07806-5000
6	RDECOM ARDEC RDAR MEF S D PANHORST G MINER R FULLERTON B DEFRAZCO M MARSH P FERLAZZO BLDG 94 PICATINNY ARSENAL NJ 07806-5000	3	RDECOM ARDEC RDAR MEF I R GRANITZKI J CHOI L VO BLDG 95 PICATINNY ARSENAL NJ 07806
4	RDECOM ARDEC RDAR MEM C D NGUYEN R GORMAN D CIMORELLI K SANTANGELO BLDG 94 PICATINNY ARSENAL NJ 07806-5000	1	US ARMY ARDEC AMSRD AAR AEM M LUCIANO BLDG 65S PICATINNY ARSENAL NJ 07806
3	US ARMY ARDEC D DEMELLA P MAGNOTTI A LICHTENBERG-SCANLON BLDG 61S PICATINNY ARSENAL NJ 07806-5000	1	US ARDEC AMSRD AAR AEP A M HOHIL BLDG 407 PICATINNY ARSENAL NJ 07806-5000
2	RDECOM ARDEC RDAR MEM M C MOEHRINGER J TRAVAILLE BLDG 94 PICATINNY ARSENAL NJ 07806-5000	4	RDECOM ARDEC AMSRD AMR SG SD J BAUMAN H SAGE S DUNBAR B NOURSE BLDG 5400 REDSTONE ARSENAL AL 35898
2	US ARMY ARDEC AMSRD AAR AEP E C STOUT D CARLUCCI BLDG 94 PICATINNY ARSENAL NJ 07806-5000	2	US ARMY TACOM ARDEC AMSRD AR AEP S N GRAY D PASCUA BLDG 94 PICATINNY ARSENAL NJ 07806-5000

<u>NO. OF COPIES</u>	<u>ORGANIZATION</u>	<u>NO. OF COPIES</u>	<u>ORGANIZATION</u>
2	PM CAS SFAE AMO CAS R KIEBLER P MANZ BLDG 171 PICATINNY ARSENAL NJ 07806	2	NAVAL SURFACE WARFARE CTR DAHlgren DIV N COOK L STEELMAN G33 6210 TISDALE RD STE 223 DAHlgren VA 22448-5114
2	PM CAS SFAE AMO CAS EX J MINUS M BURKE BLDG 171 EX PICATINNY ARSENAL NJ 07806	1	ALLIANT TECHSYSTEMS INC ALLEGANY BALLISTICS LAB S OWENS MS WV01 08 BLDG 300 RM 180 210 STATE RTE 956 ROCKET CTR WV 26726-3548
3	US ARMY ARDEC SFAE AMO CAS MS P BURKE G SCHWARTZ J HILT BLDG 162S PICATINNY ARSENAL NJ 07806-5000	1	SAIC J NORTHRUP 8500 NORMANDALE LAKE BLVD STE 1610 BLOOMINGTON MN 55437-3828
1	CDR US ARMY TACOM ARDEC SFAE AMO MAS C GRASSANO BLDG 354 PICATINNY ARSENAL NJ 07806	1	SAIC D HALL 1150 FIRST AVE STE 400 KING OF PRUSSIA PA 19406
1	US ARMY ARDEC SFAE AMO MAS LC D RIGOGLIOSO BLDG 354 PICATINNY ARSENAL NJ 07806	1	GEN DYNAMICS ST MARKS H RAINES PO BOX 222 SAINT MARKS FL 32355-0222
1	PM MAS SFAE AMO MAS SETI J FOULTZ BLDG 354 PICATINNY ARSENAL NJ 07806	1	GEN DYNAMICS ARM SYS J TALLEY 128 LAKESIDE AVE BURLINGTON VT 05401
1	FIRES DEPUTY MGR EXP MANEUVER WARFARE OFC OF NAVAL RSRCH ONR 30 875 NORTH RANDOLPH ST RM 1155B ARLINGTON VA 22203	4	BAE ARM SYS DIV T MELODY J DYVIK P JANKE B GOODELL 4800 E RIVER RD MINNEAPOLIS MN 55421-1498
		1	US ARMY YUMA PROVING GROUND TDET YPY MW M BARRON 301 C ST YUMA AZ 85365-9498

<u>NO. OF COPIES</u>	<u>ORGANIZATION</u>	<u>NO. OF COPIES</u>	<u>ORGANIZATION</u>
1	TRAX INTRNTL CORP R GIVEN BLDG 2333 YUMA PROVING GROUND AZ 85365		S SILTON P WEINACHT RDRL WML F R BITTING F BRANDON B DAVIS T HARKINS D HEPNER M ILG G KATULKA D LYON J MALEY R MCGEE C MILLER P MULLER P PEREGINO D PETRICK B TOPPER RDRL WML G
1	ARROW TECH ASSOC W HATHAWAY 1233 SHELBURNE RD STE D-8 SOUTH BULINGTON VT 05403		
1	GEORGIA INST OF TECHLGY SCHOOL OF AEROSPACE ENG M COSTELLO ATLANTA GA 30332		
<u>ABERDEEN PROVING GROUND</u>			
6	COMMANDER US ARMY TACOM ARDEC AMSRD AR AEF D R LIESKE J MATTIS A SOWA J FONNER M ANDRIOLI B NARIZZANO		T BROWN W DRYSDALE M MINNICINO J BENDER RDRL WML H C CANDLAND M FERMEN-COKER R SUMMERS RDRL WMP F N GNIAZDOWSKI
47	DIR USARL RDRL WM P PLOSTINS RDRL WML M ZOLTOSKI J NEWILL RDRL WML A W OBERLE R PEARSON L STROHM RDRL WML D J SCHMIDT M NUSCA RDRL WML E I CELMINS G COOPER J DESPIRITO L FAIRFAX F FRESCONI (5 CPS) J GARNER B GUIDOS B HOWELL G OBERLIN J SAHU		